



## Synthesis and characterization of novel calcined ferrihydrite-modified diatomite (FMD3X6) and its UVA light-assisted heterogeneous photodegradation of VG3 dye

Walid Rezig<sup>a,b</sup>, Abdelkader Elaziouti<sup>a,b,\*</sup>, Nadja Laouedj<sup>b,c</sup>, Mohamed Hadjel<sup>a,b</sup>

<sup>a</sup>Laboratoire des Sciences, Technologie et Génie des Procédés (L.S.T.G.P.), emails: abdelkader.elaziouti@univ-usto.dz/elaziouti\_a@yahoo.com (A. Elaziouti), walid.rezig@univ-usto.dz (W. Rezig), mohamed.hadjel@univ-usto.dz (M. Hadjel)

<sup>b</sup>Université des sciences et de la technologie d'Oran Mohammed Boudiaf (USTO M.B), BP 1505 El M'naouar 31000, Oran, Algérie, email: nadja.laouedj@univ-usto.dz (N. Laouedj)

<sup>c</sup>Laboratoire des Matériaux Inorganiques et Application (L.M.I.A)

Received 10 February 2022; Accepted 11 July 2022

---

### ABSTRACT

A novel ferrihydrite-modified diatomites (FMD3) and its calcined phase at 600°C/24 h (FMD3X6) were successfully synthesized and developed for degradation of vat green 3 indanthrene from aqueous solution under UVA light irradiation. The as-prepared RD (raw diatomites), FMD3 and FMD3X6 were characterized by X-ray fluorescence spectroscopy, X-ray diffraction, attenuated total reflectance-Fourier-transform infrared spectroscopy, scanning electron microscope-energy-dispersive X-ray (SEM-EDX), thermogravimetric analysis-differential scanning calorimetry and UV-Vis-DRS (diffuse reflectance spectroscopy), X-ray photoelectron spectroscopy techniques. The performance of heterogeneous photocatalysis process was investigated under two key parameters: reaction time and pH medium. Results revealed that FMD3X6 possessed multicrystalline phases: SiO<sub>2</sub>, γ-FeOOH, α-Fe<sub>2</sub>O<sub>3</sub>, γ-Fe<sub>2</sub>O<sub>3</sub> and CaCO<sub>3</sub>. The average crystallite size of RD, FMD3 and FMD3X6 were 106.105, 90.890 and 116.448 nm, respectively. According to the Sears process, the surface area value of RD (307.8 m<sup>2</sup> g<sup>-1</sup>) was higher than these of FMD3 (195.8 m<sup>2</sup> g<sup>-1</sup>) and FMD3X6 (218.2 m<sup>2</sup> g<sup>-1</sup>). The band gap were found to be 2.48, 1.45 and 1.25 eV for RD, FMD3 and FMD3X6, respectively, while the pH<sub>PZC</sub> were found to be 5 for RD and 6 for the both FMD3 and FMD3X6. SEM observation indicated that colloidal-size ferrihydrites are deposited in diatomite macropores and/or larger mesopores. The binding energies of Fe 2p<sub>1/2</sub>, Fe 2p<sub>3/2</sub> and O 1s of FMD3X6 catalyst implied that the α-Fe<sub>2</sub>O<sub>3</sub> phase is combined on the interface of diatomite via Fe–O–Si bond. The predicted Brunauer–Emmett–Teller specific surface area and the average pore diameter of FMD3X6 are estimated to be 2.1 m<sup>2</sup> g<sup>-1</sup> and 1.9 nm, respectively. Up to 92% degradation of VG3 was achieved within 1 h at pH = 10 at 25°C and the kinetics of photocatalytic degradation of VG3 are well adjusted with pseudo-first-order kinetic model. The primarily reason for the enhanced photocatalytic efficiency of FMD3X6 matrix is ascribed to the generated powerful oxidizing agents (h<sup>+</sup> and •OH), which attack organic molecules causing the chain cleavage and oxidation reactions of dye molecules.

*Keywords:* Diatomite; Ferrihydrite; Heterogeneous photocatalysis; Band gap

---

\* Corresponding author.

## 1. Introduction

Diatoms are a crucial component of phytoplankton populations in many lakes worldwide and marine environments. Accumulations of diatoms are known from all aquatic environments including wetlands, lakes, and the marine environment [1]. The kieselguhr and sand reserves are situated in Sig region (Mascara, West of Algeria) [2]. Diatomite, as an environmentally friendly and a very inexpensive material, is used for the manufacture of cements, clay diet, bricks, adsorbents, filter powders, fillers filler, abrasive and surface cleaning material, catalyst support for the production of biodiesel [3], natural insecticide or grain protectant [4] and catalyst foundation for the removal of contaminants [5]. The principal features of the diatomite are its ordered pore-size distribution and high permeability, as well as outstanding mechanical, thermal and chemical stabilities. In addition, diatomite is an fascinating immobilization support owing to the presence of the reactive groups such as silicon hydroxyl, acid sites (iron or aluminium oxides) and hydrogen bonds on the surface of amorphous  $\text{SiO}_2$  (Fig. 1) [6]. Metal oxides, minerals (mainly carbonates), clays, salts and organic matter, presented as impurities species on the diatomaceous surface, constrains the application of the latter and which can cause inconvenience in industrial applications.

To overcome the above inherent discrepancy, different strategies have been designed and to modify diatomite by using surfactants or inorganic coatings [7–9], organosilane modification occurring mesoporous/macroporous diatomite via surface silylation [10]. Diatomite respectively modified by  $\text{Zn}_2\text{SiO}_4$  [11],  $\text{Mg}_3\text{Si}_4\text{O}_{10}(\text{OH})_2$ ,  $\text{MgFe}_2\text{O}_4$  [12],  $\text{MgO}$  [13],  $\text{CuCl}$  [14], Pani [15], niobates ( $\text{MnNb}_2\text{O}_6$ ,  $\text{SnNb}_2\text{O}_6$  and  $\text{ZnNb}_2\text{O}_6$ ) [16], chitosan/amine [17],  $\text{TiO}_2$  anatase [18],  $\text{TiO}_2$ /amorphous silica minerals [19],  $\text{Ag}_3\text{PO}_4$  [20,21],  $\text{AgCl}/\text{Ag}_3\text{PO}_4$  [22] for removing heavy metals ions (Pb, Cd, Cr, Hg, As(V), Hg(II) ions), carbon monoxide (CO) adsorption and organic dyes (Rhodamine B; RhB and Methyl orange; MO) and target molecule (bisphenol A) to make it versatile for both adsorption, filtering and photocatalysis processes.

In our earlier work, we have designed  $\text{TiO}_2$ -calcined ferrihydrite-modified diatomite composite, demonstrating an excellent degradation efficiency of the vat orange 2 (VG2) [23]. In the present study, diatomite was modified through

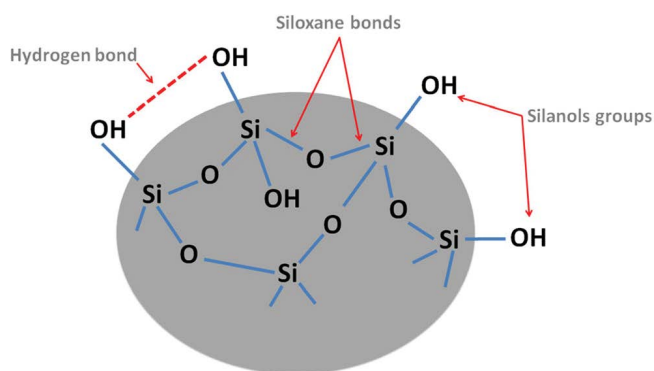


Fig. 1. Structure of diatomite surface.

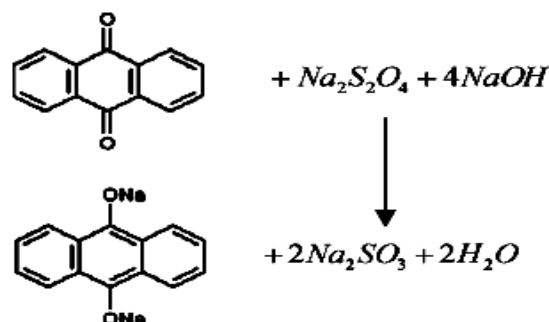
a facile method by sodium hydroxide and ferrous chloride tetrahydrate ( $\text{FeCl}_2 \cdot 4\text{H}_2\text{O}$ ). The thermal, crystallographical, morphological, functional and optical characteristics of  $\text{FeCl}_2 \cdot 4\text{H}_2\text{O}$ /diatomite catalysts were substantively characterized by thermogravimetric analysis-differential scanning calorimetry (TGA-DSC), X-ray fluorescence spectroscopy (XRF), X-ray diffraction (XRD), attenuated total reflectance-Fourier-transform infrared spectroscopy (ATR-FTIR), scanning electron microscope-energy-dispersive X-ray (SEM-EDS), UV-Vis-DRS (diffuse reflectance spectroscopy) and X-ray photoelectron spectroscopy (XPS) technique. The photocatalytic performance of  $\text{FeCl}_2 \cdot 4\text{H}_2\text{O}$ /diatomite catalyst was assessed by the photodegradation of Indanthrene Olive Green B dye (VG3), as probe organic pollutants, in simulated aqueous solution under artificial UVA light illumination. The effect of processing parameter such as pH solution on the photodegradation process was systematically investigated in details. The mechanism of photocatalytic environmental pollutant degradation application using UVA light radiation has been highlighted.

## 2. Experimental and method

### 2.1. Materials

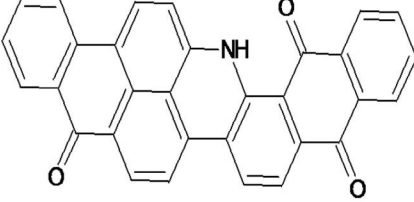
Ferrous chloride tetrahydrate ( $\text{FeCl}_2 \cdot 4\text{H}_2\text{O}$ ;  $\geq 98.0\%$ , AR), sodium hydroxide ( $\text{NaOH}$ ;  $\geq 98\%$ , AR) and Hydrogen chloride ( $\text{HCl}$ ;  $\geq 98\%$ , AR) were obtained from Sigma-Aldrich Co., (Saint-Louis, USA).

The vat green 3 indanthrene (VG3) dye was provided from the Textile Company "SOITEX-HAM" Essenia Industrial Zone, Oran, Algeria. Vat dyes, like indanthrene or indigo are practically insoluble in water, but can be reduced in the presence of an alkali and a reducing agent, like sodium dithionite ( $\text{Na}_2\text{S}_2\text{O}_4$ ) through a reduction reaction [24]. These water insoluble vat dyes are converted to soluble anthrahydroquinone compounds (leuco dye) [25], which have a certain affinity to cellulosic fibers. This conversion is represented in the following reaction.



The reduced dyestuff penetrates into the fiber (decreasing concentration of dyestuff in dyebath) and is reoxidized on the fiber back to the insoluble form which remains fixed in place. The reducing property of sodium dithionite is due to the evolution of hydrogen when dissolved in water or sodium hydroxide ( $\text{NaOH}$ ) [26]. However, the disadvantage of sodium dithionite, it is considered environmentally unfavourable since it produces sulphite,

Table 1  
Molecular structure and physical properties of the Indanthrene Olive Green B dye (VG3)

|   |   |   |
|---|---|---|
|  | CAS number                              | 3271-76-9                                       |
|   | C.I.                                    | 69500   |
|   | Chemical name                           | Vat Green 3                                     |
|   | Chemical formula                        | C <sub>31</sub> H <sub>15</sub> NO <sub>3</sub> |
|   | Molecular weight (g mol <sup>-1</sup> ) | 449.46  |
|   | Boiling point                           | 557.88°C (rough estimate)                       |
|   | Density                                 | 1.2566 (rough estimate)                         |
|   | Refractive index                        | 1.6310 (estimate)                               |
|   | pKa                                     | -2.68 ± 0.20 (predicted), 7.7                   |
|   | Chemical class                          | Anthraquinones                                  |

C.I.: Color index; CAS: Chemical Abstracts Service.

sulphate, thiosulphate and toxic sulphides as degradation products, which then contaminate the wastewaters from the dyeing plants [27].

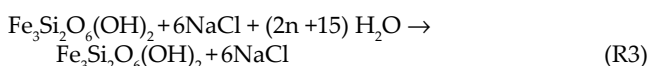
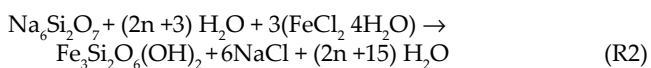
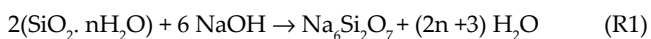
The molecular structure and physical properties of VG3 dye are presented in Table 1.

### 2.2. Preparation of VG3 stock solution

VG3 aqueous solution was made from a 1 g L<sup>-1</sup> stock solution, and the discharge was diluted to 0.5 mg L<sup>-1</sup> since it is very concentrated. Both photo-discolouration experiments on VG3 were carried out in a beaker of 250 mL with stirring at 25°C [28].

### 2.3. Preparation of ferrihydrite-modified diatomite

To partially dissolve Si, 45 g of raw diatomite (RD) impregnated within 300 mL of 6 M NaOH solution for 2 h at 90°C (Reaction R1) [29]. The impregnated mixture was subsequently added to 300 mL of 3 M FeCl<sub>2</sub>·4H<sub>2</sub>O solution, vigorously stirred and oxidized in air for 24 h at 25°C (Reaction R2). The resulting mixture was filtered, washed several times with distilled water and left to oxidize in the air for further 24 h at room temperature. After that, it was further filtered to remove the remained NaOH and further washed with distilled water to begin the oxidation of Fe(OH)<sub>2</sub> in air for 24 h and eliminate the excess NaOH oxidized (designed as FMD3). This product was dried for 24 h at 105°C and heat treated in an oven for 24 h at 600°C (Reaction R3) (designed as FMD3X6).



### 2.4. Characterizations

Elemental analysis on RD and FMD3X6 was carried out by (Bruker S1 Titan X-ray fluorescence, Billerica, Massachusetts, USA) XRF spectrometer. TGA and DSC were recorded on

a (STD Q600 V.3 Build 101, TA instruments, New Castle, USA). At a heating rate of 10°C/min under nitrogen (N<sub>2</sub>) atmosphere in the temperature range of 0°C–900°C (for RD) and 0°C–1,200°C (for FMD3X6). XRD analysis was performed by a (Bruker D8 Advance model) Cu-Kα radiation (λ = 0.1540598 nm) at low speed of rotation (0.02° s<sup>-1</sup>) over 10°–80°. The average crystallite size of RD, FMD and FMD3X6 materials is calculated from the Scherrer equation [30].

$$D_{\text{XRD}} = \frac{K \lambda}{\beta \sin \theta} \quad (1)$$

where  $D_{\text{XRD}}$  is the average crystallite size of the material (nm), λ is the X-ray wavelength (1.5406 Å), β is the full width at half maximum (FWHM) of the peaks (°), 2θ is the Bragg angle (°) and  $k$  is the shape factor (0.9). ATR-FTIR spectra were achieved using a (Bruker Model) spectrophotometer over a range of 400 to 4,000 cm<sup>-1</sup>. Elemental compositions were carried out using a (JEOL JSM-6610, Akishima, Tokyo, Japan) scanning electron microscope (SEM) connected with an energy-dispersive X-ray (EDX) device. Optical absorption spectra were recorded on the (PerkinElmer Lambda 650, Waltham, Massachusetts, USA) spectrophotometer linked to an integrating sphere assembly (UV-Vis-DRS). Differential pore-size distributions and nitrogen adsorption–desorption isotherms of FMD3X6 sample was determined at 77 K using Micromeritics adsorption equipment (Model Gemini VII Version 3.04 Serial # 881 Unit 1, Gemini Model 2390t, Micromeritics Instruments Corp., USA) by using the Brunauer–Emmett–Teller (BET) method and assuming a cross-sectional area of each nitrogen molecule of 0.162 nm<sup>2</sup>. Before nitrogen adsorption, a sample (≈0.3 g) was degassed at 473 K for 3 h at a vacuum of 5 × 10<sup>-4</sup> atm to remove adsorbed moisture from the sample surface and pores.

XPS measurements were recorded on a (Kratos Axis Ultra) using Al<sub>Kα</sub> (1,486.6 eV) radiation. High resolution spectra were acquired at 20 eV pass energy with energy resolution of 0.9 eV. The C 1s line of 284.4 eV was used as a reference to correct the binding energies for charge energy shift. A Shirley background was subtracted from the spectra and signals; symmetric Gaussian functions were used in the peak fitting procedure.

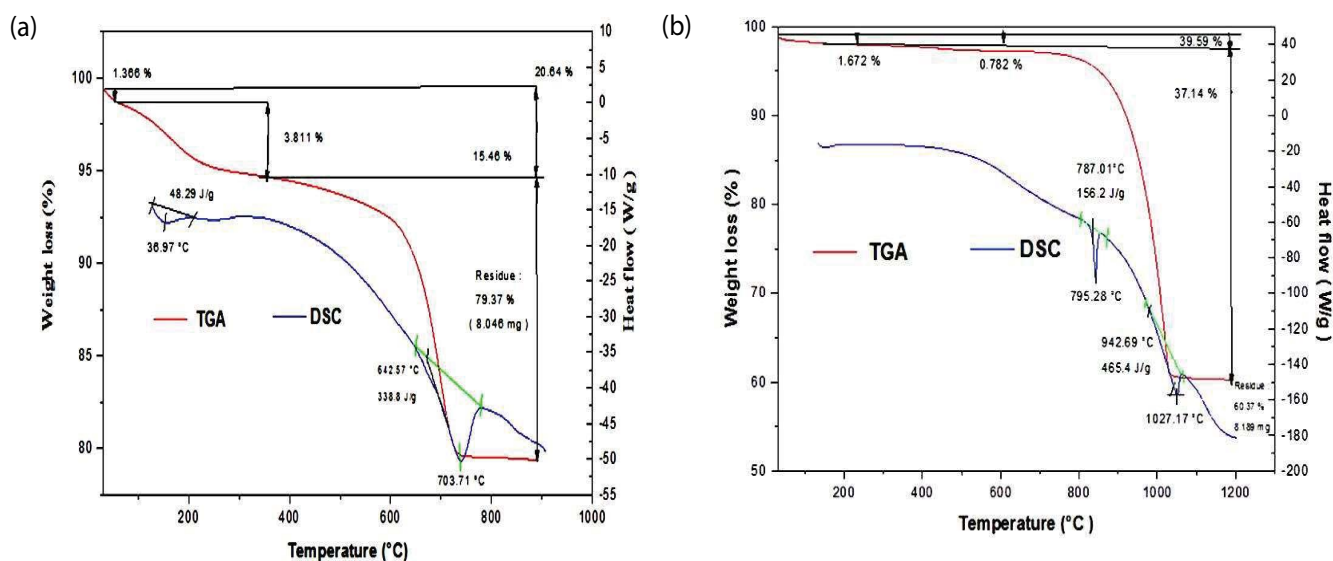


Fig. 2. TGA-DSC diagrams of (a) RD and (b) FMD3X6.

### 2.5. Surface area of RD and FMD using Sears's method

The surface area of the diatomite was determined, according to Sears' method [31],

In a typical assay: 0.5 g of FMD3X6 were acidified to a pH of 3–3.5 by HCl solution and then 50 mL with distilled water and 10 g of NaCl were added under constant magnetic stirring. The solution pH was adjusted with 0.1 M NaOH. The amount volume needed to raise pH from 4 to 9 was measured. Thus, the surface area ( $S$ ) was calculated using the Sears's formula [32]:

$$S(\text{m}^2\text{g}^{-1}) = 32V - 25 \quad (2)$$

where  $V$  is the volume required to raise pH, 32 and 25 are Sears empiric constants.

### 2.6. Surface charge

To assess the surface charge of RD, FMD3 and FMD3X6 materials, the potentiometric titration method was employed. Diatomite materials (mass concentration around  $1 \text{ g L}^{-1}$ ) were stirred for 2 h at  $25^\circ\text{C}$ . Titrations were then carried out by using 0.1 M (HCl and/or NaCl solution), with the pH being tracked throughout. The volume of the titrating acid or base agents required to modify the pH from 3 to 12 was collected, duplicate samples were calculated, and the results were averaged.

The following equations specify the surface charge density ( $\text{C m}^{-2}$ ) [33,34]:

$$\sigma = (C_A - C_B + [[\text{OH}^-] - [\text{H}^+]])F / A m \quad (3)$$

where  $C_A$  and  $C_B$  are the acid and base molar concentrations required to achieve a point on the titration curve, ( $\text{mol L}^{-1}$ ),  $[\text{H}^+]$  and  $[\text{OH}^-]$  are the  $\text{H}^+$  and  $\text{OH}^-$  concentrations converted from pH ( $\text{mol L}^{-1}$ ),  $F$  is the Faraday constant ( $96,490 \text{ C mol}^{-1}$ ),

$A$  is the real surface area ( $\text{m}^2 \text{g}^{-1}$ ), and  $m$  is the RD or FMD3X6 mass concentration ( $\text{g L}^{-1}$ ).

### 2.7. Photocatalytic experiments

In this study, the impact of pH solution (4, 7 and 10) on the photocatalytic efficiency of RD and FMD3X6 for the degradation of VG3 dye in the simulated aqueous solution under UVA light irradiation was investigated. In typical assay, a known amount of RD or FMD3X6 powder (mass/volume ratio of  $0.5 \text{ g L}^{-1}$ ) was mixed with VG3 solution ( $100 \text{ mL}$ ;  $10 \text{ mg L}^{-1}$ ) in a pyrex vessel at  $25^\circ\text{C}$  and adjusted to pH 10 by using NaOH solution. The suspension was then kept in the dark for 60 min to attain the adsorption/desorption equilibrium, then the solution was exposed to the ultraviolet A ( $15 \text{ W}$ ;  $\text{UVA} = 365 \text{ nm}$ ) light irradiation under continuous stirring. Afterward, for each assay, aliquots of the suspension were withdrawn and then recovered by centrifugation ( $15,000 \text{ rpm}$  for 15 min). The dye residual concentrations of the resulting solutions during the photodegradation process were then monitored on Optizen Micrometrics spectrophotometer.

The photo degradation efficiency  $\eta$  (%) of RD and FMD3X6 materials were assessed according the following expression:

$$\eta(\%) = \left[ \frac{(C_0 - C_t)}{C_0} \right] 100 \quad (4)$$

where  $C_0$  symbolizes the initial concentration of VG3 ( $\text{mg L}^{-1}$ ) at time  $t = 0 \text{ min}$  and  $C_t$  denotes the residual concentration of VG3 ( $\text{mg L}^{-1}$ ) at irradiation time  $t$ .

The photocatalytic degradation of VG3 on diatomites materials was analyzed with the pseudo-first-order kinetic model Eqs. (5) or (6):

$$C = C_0 e^{-K_1 t} \quad (5)$$

Table 2  
Mineralogical analysis in percentages by % weight of RD, FMD3 and FMD3X6

| Components        | SiO <sub>2</sub> | Fe <sub>2</sub> O <sub>3</sub> | Al <sub>2</sub> O <sub>3</sub> | CaO   | MgO  | K <sub>2</sub> O | TiO <sub>2</sub> | Na <sub>2</sub> O | P <sub>2</sub> O <sub>5</sub> | MnO  | SO <sub>3</sub> | LOI   |
|-------------------|------------------|--------------------------------|--------------------------------|-------|------|------------------|------------------|-------------------|-------------------------------|------|-----------------|-------|
| RD (%) weight     | 68.02            | 2.02                           | 7.58                           | 19.25 | 2.02 | 1.49             | 0.14             | 0.2               | –                             | 0.04 | –               | –     |
| FMD3 (%) weight   | 22.87            | 15.82                          | 4.13                           | 23.58 | 1.27 | 0.76             | 0.25             | –                 | 0.21                          | –    | 0.38            | 30.73 |
| FMD3X6 (%) weight | 37.27            | 20.14                          | 3.42                           | 1.56  | 1.30 | 1.25             | 0.25             | –                 | 0.21                          | –    | 0.14            | 34.46 |

LOI: Loss on ignition.

Or

$$\ln \frac{C}{C_0} = -K_1 t \quad (6)$$

where  $C$  (or  $C_t$ ) signifies the residual concentration of VG3 ( $\text{mg L}^{-1}$ ) at irradiation time  $t$  and  $K_1$  denotes the apparent reactions rate constant ( $\text{min}^{-1}$ ). The plot of  $\ln(C/C_0)$  vs.  $t$  for all pHs should be straight lines and the values of  $K_1$  can be deduced directly through its slope.

### 3. Results and discussion

#### 3.1. XRF analysis

Table 2 displays the chemical composition of RD, FMD3 and FMD3X6 samples. Results indicated that the main contents of RD catalyst, expressed in the term of oxides, are primarily SiO<sub>2</sub> (68.02%) and CaO (19.25%) with less Al<sub>2</sub>O<sub>3</sub> (7.58%), Fe<sub>2</sub>O<sub>3</sub> (2.02%) and MgO (2.02%). The others oxides present in traces contents (Na<sub>2</sub>O, K<sub>2</sub>O, TiO<sub>2</sub> and MnO) were determined as the main impurity. However, for FMD3 and FMD3X6 materials, an obvious inconsistency in chemical composition was observed by decreasing in silica (SiO<sub>2</sub>) content, almost reaching 22.87% and 37.27%, respectively. For FMD3, a slight decrease in Al<sub>2</sub>O<sub>3</sub> (4.13%) and Na<sub>2</sub>O (0%) contents associated simultaneously by a great increase in Fe<sub>2</sub>O<sub>3</sub> (15.82%) was observed. Meanwhile, for FMD3X6, Al<sub>2</sub>O<sub>3</sub> and Na<sub>2</sub>O contents declined to 3.42% and 0%, respectively, while Fe<sub>2</sub>O<sub>3</sub> contents was increased to 20.14%, which should be considered as reactive exchange sites of FMD3 diatomite [35]. Momentarily, CaO content was slightly increased from 19.25% (RD) to 23.58% (FMD3) and then scarily declined to 1.56% (FMD3X6). The others elements considered as main impurities such as MgO, K<sub>2</sub>O, SO<sub>3</sub>, P<sub>2</sub>O<sub>5</sub> and TiO<sub>2</sub> were noticeably reduced to 1.27%, 0.76%, 0.38%, 0.21% and 0.25%, respectively for FMD3 and to 1.30%, 1.25%, 0.14%, 0.21% and 0.24%, correspondingly for FMD3X6. The loss on ignition (LOI) in term of organic matter (OM) and carbonate content of FMD3 and FMD3X6 samples, raised up 30.73% and 34.46%, respectively. The decrease in the SiO<sub>2</sub> ratio may be accredited to relative solubility in the alkali medium, while the calcite is mostly in the form of carbonate, which decomposes easily in acidic medium through washing-oxidizing steps during the elaborating process of ferrihydrite-modified diatomite (FMD3 and FMD3X6). Thus, the CaO content has clearly decreased the addition of the acid, and finally the increase in sodium is due to the neutralization of the treated

diatomite which was made by soda. Finally, the absence of Na<sub>2</sub>O is due to the neutralization of the treated diatomite FMD3X6.

#### 3.2. TGA-DSC analysis

The thermal stability and phase changing behavior of the elaborated diatomites have been investigated by simultaneous analyses TGA-DSC in reductive atmosphere (synthetic N<sub>2</sub>). The TGA-DSC thermograms of the pristine diatomite (RD) are illustrated in Fig. 2a. As it can be seen from Fig. 2a, the first mass loss of 1.366% occurred in the temperature range of 25°C–70°C. The DSC curve of RD displays a melting temperature ( $T_M$ ) at 36.97°C and a latent heat ( $H_M$ ) of 48.29 J g<sup>-1</sup>, is attributed to the desorption of physisorbed water. The dehydroxylation of calcium hydroxide started at 70°C and finished at 230°C, which relates to the second mass losses of 3.811%. A first endothermic peak, namely at 703.71°C ( $T_M$ ) with the latent heat of 338.8 J g<sup>-1</sup> ( $H_M$ ) is also observed in the DSC curve of RD [36] along with the second peak at 703.71°C corresponds to  $\alpha \leftrightarrow \beta$  quartz transformation. The third mass loss ( $\approx 15.46\%$ ), the more important in percentage, occurred mainly between 300°C and 890°C, which is attributed to the decarbonation and dehydroxylation of silanol groups (Si–OH). The weight loss of residue crystallization is found to be 79.37%.

In the other hand, the TGA-DSC curves of FMD3X6 heated up to 1,200°C are depicted in Fig. 2b. The mass loss process of FMD3X6 is performed by three well defined steps. The first weight loss (1.672%) at 25°C–200°C range, the second mass loss (0.782%) from 200°C to 600°C and the last sharp weight loss (37.14%) occurred at 600°C–1,200°C. The total mass loss of FMD3X6 is around 39.59% through phase transition processes, which is almost two times superior than that of RD (20.64%; Fig. 2a). Besides, as depicted in Fig. 2b, FMD3X6 melts at 795.28°C ( $T_M$ ) with the latent heat of 156.2 J g<sup>-1</sup> ( $H_M$ ) and around 1,027.17°C ( $T_M$ ) with latent heat of 465.4 J g<sup>-1</sup> ( $H_M$ ). The first endothermic peak at 795.28°C ( $T_M$ ) was assigned to the decomposition of the organic matter (OM) on FMD3X6 silica surface, as well as the dehydroxylation of the silanol groups (Si–OH) upon rising the temperature [37]. However, the second endothermic peak at 1,027.17°C ( $T_M$ ) is caused by the transition of FMD3X6 ferrihydrite to hematite ( $\alpha\text{-Fe}_2\text{O}_3$ ) or crystallization of  $\alpha\text{-Fe}_2\text{O}_3$  above 300°C [38]. The last phase change was completed by the dehydroxylation step, which overlaps with instantaneous crystallization of the end hematite product from disordered to crystalline ( $\alpha\text{-Fe}_2\text{O}_3$ ) [39–42]. The first phase transition temperature of FMD3X6 is about

787.01°C and the second phase transition temperature is around 942.69°C. The weight loss of residue crystallization is found to be 60.37% (8.189 mg). A comparison of thermal characteristics between RD and FMD3X6 deduced from TGA-DSC assessment are summarized in Table 3.

### 3.3. XRD analysis

Fig. 3 illustrates XRD of RD, FMD3 and FMD3X6 materials. The diffraction peaks were exhibited at  $2\theta = 20.83^\circ, 26.63^\circ, 39.42^\circ, 50.09^\circ, 57.34^\circ, 59.96^\circ, 64.75^\circ$  and  $68.32^\circ$  on the XRD pattern of RD correspond to (100), (011), (012), (112), (210), (121), (113) and (203) crystal face of  $\text{SiO}_2$  [25], indicating that the diatomite is a porous  $\text{SiO}_2$  nature. The diffraction peaks at  $2\theta = 23.13^\circ, 29.41^\circ, 30.93^\circ, 35.95^\circ, 43.16^\circ, 47.5^\circ$  and  $48.5^\circ$  are assigned to ((012), (104), (006), (110) (202), (018) and (116) crystal face of pure  $\text{CaCO}_3$  (JCPDS5-586), respectively. The broad peak over a  $2\theta$  range of  $20^\circ$ – $30^\circ$  reveals a typical amorphous structure of pristine RD. Moreover, there are notable diffraction peaks at around  $2\theta = 26.63^\circ$  and  $29.41^\circ$ , matching to quartz and calcite phases, respectively. In addition, another small diffraction peaks are also observed in the XRD of RD, belonging to  $\text{Al}_2\text{O}_3$ ,  $\text{Fe}_2\text{O}_3$ ,

$\text{K}_2\text{O}$ ,  $\text{MgO}$ ,  $\text{Na}_2\text{O}$ ,  $\text{TiO}_2$ , and  $\text{MnO}$ , in well accordance with XRF results.

Conversely, five notable sharp reflections at  $2\theta = 24.1^\circ, 27.43^\circ, 49.43^\circ, 56.43^\circ$  and  $66.2^\circ$  with  $d$ -spacing  $d = 0.368, 0.325, 0.184, 0.162$  and  $0.141$  nm were detected in the XRD pattern of FMD3 and FMD3X6, correspond to lepidocrocite ( $\gamma\text{-FeOOH}$ ) crystal structure (JCPDS 8-98). Two diffraction peaks at  $2\theta = 33.13^\circ$  and  $54.03^\circ$  with  $d$ -spacing =  $0.27$  and  $0.169$  nm, respectively, are assigned to hematite ( $\alpha\text{-Fe}_2\text{O}_3$ ) trigonal crystal (JCPDS 13-534), while another main peak at around  $43^\circ$  with  $d = 0.251$  nm, belongs to maghemite ( $\gamma\text{-Fe}_2\text{O}_3$ ) cubic crystal in ferrihydrite-modified diatomite (JCPDS 39-1346). The peak at  $2\theta = 45.41^\circ$  with  $d = 3.68$  nm corresponds to quartz ( $\text{SiO}_2$ ) hexagonal crystal (JCPDS 5-490).  $\text{CaCO}_3$  rhombohedral crystal is represented by the peak at  $2\theta = 31.66^\circ$  with  $d = 0.282$  nm (JCPDS 5-586).

The average crystallite size of RD, FMD3 and FMD3X6, calculated from data of FWHM of the prominent peak using the Scherrer's formula, are equal to 106.105, 90.890 and 116.448 nm, respectively. Tables 4–6 summarize the crystallographic properties of RD, FMD3 and FMD3X6 catalysts, respectively.

Based on the Sears process, the surface area values of RD, FMD3 and FMD3X6 catalysts used in this analysis are 307.8, 195.8, and 218.2  $\text{m}^2 \text{g}^{-1}$ , respectively.

Table 3  
Thermal characteristics of the RD and FMD3X6 “phase change diatomite”

| Sample | Total weight loss (wt.%) | Melting process             |                            |
|--------|--------------------------|-----------------------------|----------------------------|
|        |                          | $H_M$ ( $\text{J g}^{-1}$ ) | $T_M$ ( $^\circ\text{C}$ ) |
| RD     | 20.64                    | 48.29                       | 36.97                      |
|        |                          | 338.8                       | 703.71                     |
| FMD3X6 | 39.59                    | 156.2                       | 795.28                     |
|        |                          | 465.4                       | 1,027.17                   |

Table 4  
Crystallographic parameters of RD

| $2\theta$ ( $^\circ$ ) | $hkl$   | $\theta$ ( $^\circ$ ) | FWHM, $\beta$ (radians) | $D_{\text{XRD}}$ (nm) | $d$ -spacing (nm) |
|------------------------|---------|-----------------------|-------------------------|-----------------------|-------------------|
| 26.63                  | (0 1 1) | 13.31                 | 0.001343                | 106.105               | 0.334             |
| 29.41                  | (1 0 4) | 14.70                 | 0.002023                | 70.861                | 0.303             |
| 39.42                  | (0 1 2) | 19.71                 | 0.002703                | 54.488                | 0.228             |
| 43.16                  | (2 0 2) | 21.58                 | 0.001639                | 90.962                | 0.209             |

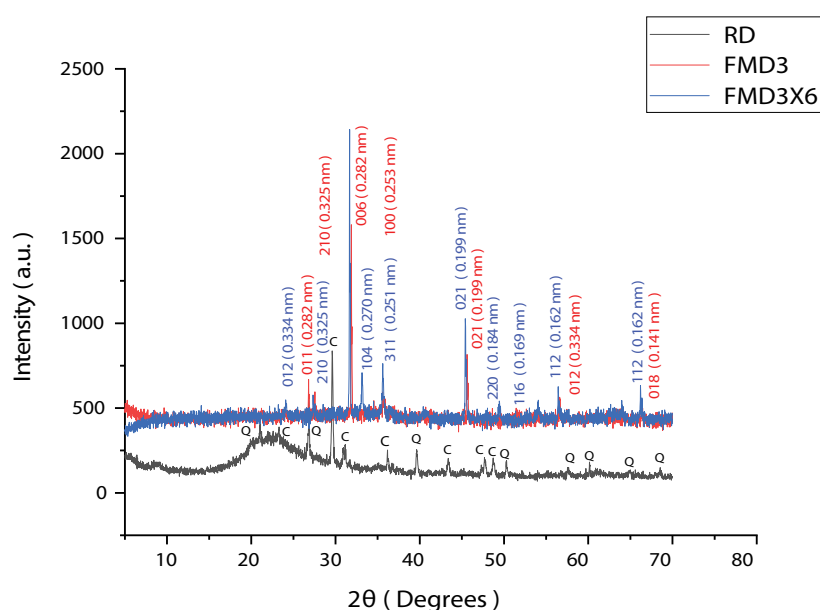


Fig. 3. XRD of RD, FMD3 and FMD3X6.



### 3.4. ATR-FTIR analysis

ATR-FTIR spectra of RD (Fig. 4a), FMD3 (Fig. 4b), and FMD3X6 (Fig. 4c), respectively, are also investigated. It can be seen from Fig. 4a, that bands positioned at 3,999; 3,444.24 and 1,622.78  $\text{cm}^{-1}$  corresponded to the O–H symmetric/antisymmetric stretching, and H–O–H bending vibrations of physically adsorbed water on H-bonded silanol groups (Si–OH). Besides, bands centred at 1,633.41; 1,645.95; 1,101.15 and 1,027.87  $\text{cm}^{-1}$  were attributed to the vibrations

Table 5  
Crystallographic parameters of FMD3

| $2\theta$ ( $^\circ$ ) | <i>hkl</i> | $\theta$ ( $^\circ$ ) | FWHM, $\beta$ (radians) | $D_{\text{XRD}}$ (nm) | <i>d</i> -spacing (nm) |
|------------------------|------------|-----------------------|-------------------------|-----------------------|------------------------|
| 26.60                  | (0 1 1)    | 13.30                 | 0.0013433               | 106.097               | 0.334                  |
| 27.35                  | (2 1 0)    | 13.67                 | 0.0020235               | 70.540                | 0.325                  |
| 31.66                  | (0 0 6)    | 15.83                 | 0.0012385               | 116.399               | 0.282                  |
| 35.54                  | (1 0 0)    | 17.77                 | 0.0052355               | 27.817                | 0.253                  |
| 45.53                  | (0 2 1)    | 33.17                 | 0.0012385               | 121.444               | 0.199                  |
| 56.44                  | (1 1 2)    | 22.76                 | 0.0012385               | 127.098               | 0.162                  |
| 66.21                  | (0 1 8)    | 33.10                 | 0.0024771               | 66.8353               | 0.141                  |

of Si–O–Si, while the band located at 877.452  $\text{cm}^{-1}$  matched up to the stained vibration of the silanol group. Moreover, the band at 803.206  $\text{cm}^{-1}$  related to the vibration of (Al–O–Si). In the other hand, ATR-FTIR spectrum of FMD3X6 (Fig. 4b) exhibits a band at 3,398.47  $\text{cm}^{-1}$  corresponded to monomeric hydrogen bonds, which are assigned to Fe–OH species on the surface in the FMD3X6 system [43] and two others bands situated at 713.25, 683.64 and 641.04  $\text{cm}^{-1}$  were assigned to the Si–O–Fe/Ti–O and Fe–O–Fe respectively. Additionally, surface iron atoms appear to complete their coordination shell by reacting with water molecules to form surface Fe–OH species in nano-hydroxylated atoms. Additionally,

Table 6  
Crystallographic parameters of FMD3X6

| $2\theta$ ( $^\circ$ ) | <i>hkl</i> | $\theta$ ( $^\circ$ ) | FWHM, $\beta$ (radians) | $D_{\text{XRD}}$ (nm) | <i>d</i> -spacing (nm) |
|------------------------|------------|-----------------------|-------------------------|-----------------------|------------------------|
| 31.66                  | (0 0 6)    | 15.83                 | 0.001238                | 116.448               | 0.282                  |
| 33.13                  | (1 0 4)    | 16.56                 | 0.001692                | 85.521                | 0.270                  |
| 35.59                  | (3 1 1)    | 17.79                 | 0.001692                | 86.089                | 0.251                  |
| 45.41                  | (0 2 1)    | 22.70                 | 0.002703                | 55.631                | 0.199                  |
| 56.43                  | (1 1 2)    | 28.21                 | 0.001639                | 96.045                | 0.162                  |

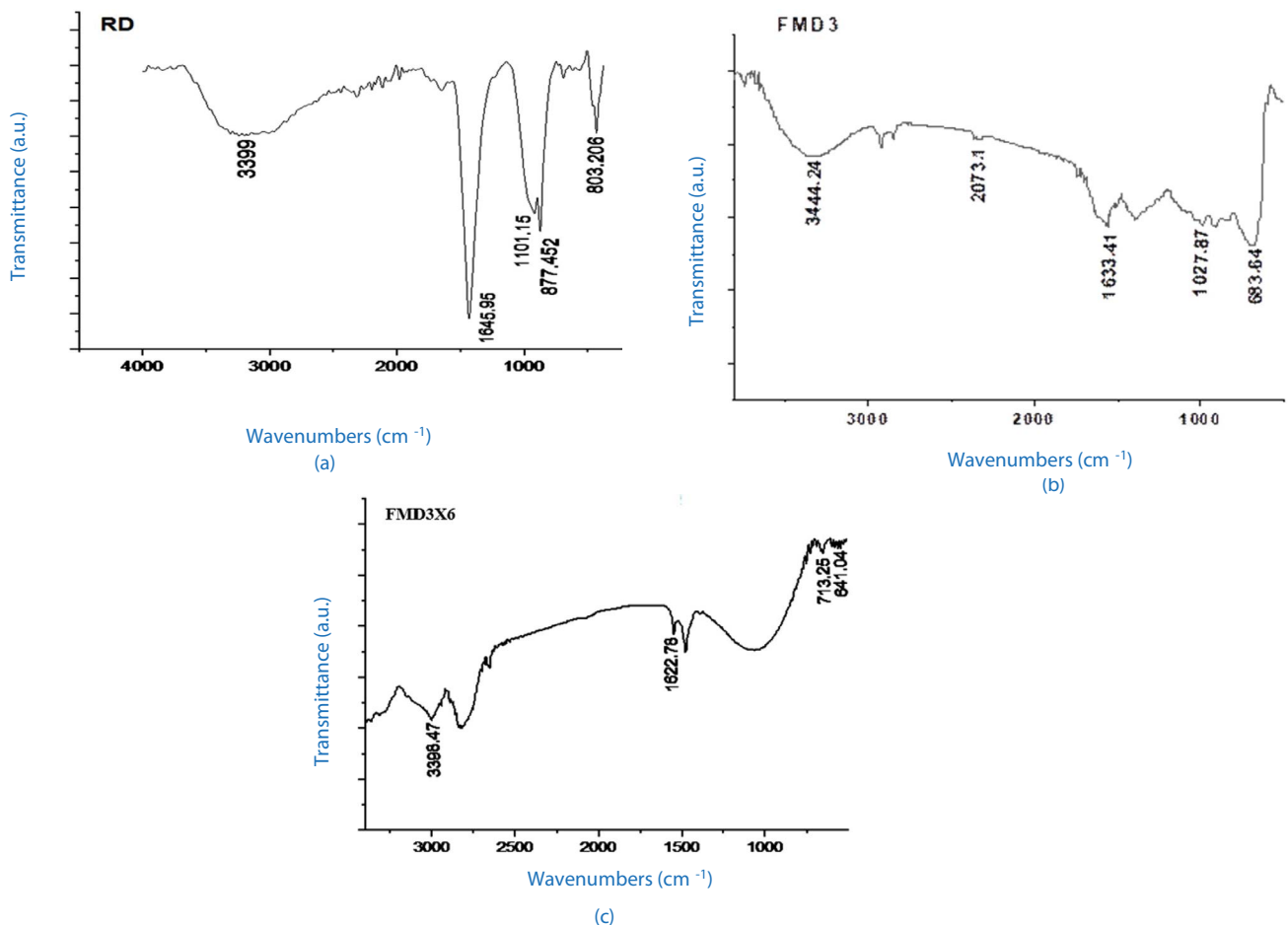


Fig. 4. ATR-FTIR spectra of (a) RD, (b) FMD3 and (c) FMD3X6.

the bands at  $2,073.1\text{ cm}^{-1}$  is unambiguously assigned to C–O stretching mode ( $\nu_{\text{C-O}}$ ) of calcium carbonate [44,45].

### 3.5. UV-Vis-DRS analysis

Figs. 5 and 6 illustrate optical absorption spectra of the VG3, RD, FMD3 and FMD3X6 catalysts over wavelength range 200–1,000 nm. RD sample shows two distinct absorption bands in the ultraviolet region at around 260 and 360 nm, assigned to a low-energy charge transfer between the oxygen ligands and the central  $\text{Fe}^{3+}$  ion in tetrahedral symmetry. A broad band was observed in the visible region. Compared to the absorption spectrum of RD, the absorption band of FMD3 catalyst increased and became broad with  $\text{FeCl}_2 \cdot 4\text{H}_2\text{O}$ . A slight shift of the absorption edge towards lower energy was observed. The absorption intensity of FMD3X6 matrix is slightly improved in the visible region upon incorporation of  $\text{FeCl}_2 \cdot 4\text{H}_2\text{O}$  into diatomite and heated up  $600^\circ\text{C}$ . The observed redshift can be related to the implantation of the energy levels within the conduction band (CB). Additionally, the broad absorption band centered at 850 nm is observed probably due to the presence of octa-coordinated extra-framework species and  $\text{Fe}_2\text{O}_3$  species [46]. The features collected so far supports the assumption that the majority of the iron atoms exist tetrahedral coordinated within the diatomite.

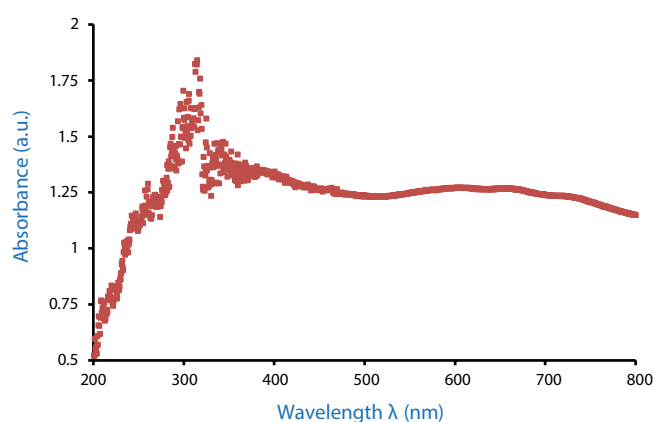


Fig. 5. UV-Vis-DRS spectrum of VG3.

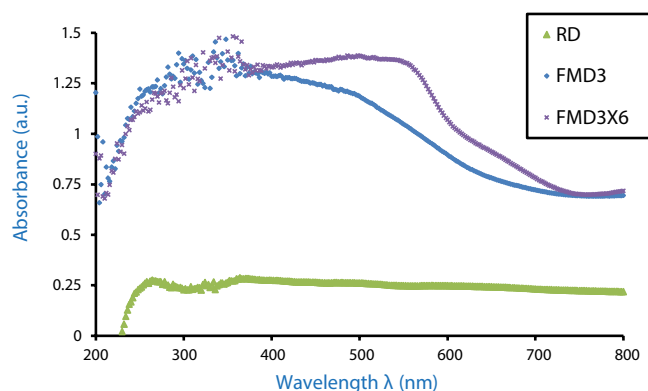


Fig. 6. UV-Vis-DRS spectra of RD, FMD3 and FMD3X6.

Moreover, the red shift at around 900 nm, demonstrating the visible light stimulation of FMD3 and FMD3X6. Table 7 reports the optical properties of the RD, FMD3 and FMD3X6 and their corresponding band gap energy ( $E_g$ ) calculated by the Planck's Law and Kubelka–Munk theory [47].

According to the Planck's Law, the absorption wavelength of the photoreactor can be done by determining its band gap value  $E_g$  (eV) using Eq. (7):

$$E_g = \frac{hc}{\lambda} = \frac{1239}{\lambda} \quad (7)$$

where  $h$  is Planck's constant ( $4.13566733 \times 10^{-15}$  eV·s);  $c$  is the speed of light ( $2.99792458 \times 10^{17}$  nm  $\text{s}^{-1}$ ) and  $\lambda$  is the wavelength (nm).

The working form of the Kubelka–Munk relationships [Eqs. (8) and (9)] used are.

$$\alpha \cong \frac{(1-R^2)}{2R} \quad (8)$$

and

$$R \cong 10^{-A} \quad (9)$$

where  $\alpha$  is linear absorption coefficient,  $R$  is the reflectance and  $A$  is the absorbance.

Tauc's equation [Eq. (9)] has been used to get the band gap value for VG3, RD, FMD3 and FMD3X6) [48].

$$(\alpha h\nu)^{1/n} \cong A(h\nu - E_g) \quad (10)$$

where  $\nu$  is the frequency of the light,  $E_g$  is the optical energy of the material and  $A$  is a material constant. The  $n$  factor is dependent on the electron transition's type and is equal to 0.5 or 2 for the direct and indirect transition band gaps, respectively.

The adsorption onset wavelength of RD, FMD3 and FMD3X6 is determined by plotting  $(\alpha h\nu)^{1/2}$  vs.  $h\nu$  and by fitting absorption data to the indirect transition ( $n = 2$ ), which are displayed in Fig. 7 and Table 7. By extrapolating the horizontal portion of  $(\alpha h\nu)^{1/2}$  vs.  $h\nu$  plot with  $x$ -axis at  $(\alpha h\nu)^2 = 0$ , the corresponding  $E_g$  is around 1.45 and 1.25 for FMD3 and FMD3X6, respectively. The decrease in  $E_g$  for FMD3X6 is possibly attributed to the incorporation impact of ferrihydrite in the diatomite matrix which increase its absorption in the visible light region.

The band edge positions  $E_{\text{CB}}$  and  $E_{\text{VB}}$  of diatomite materials are evaluated by using the geometric mean electronegativity method, which are presented by Eqs. (11) and (12) [49].

$$E_{\text{VB}(\text{vsNHE})} = \chi + 0.5E_g - 4.5 \quad (11)$$

$$E_{\text{CB}(\text{vsNHE})} = \chi - 0.5E_g - 4.5 \quad (12)$$

where  $\chi$  is absolute electronegativity (eV) and  $E_g$  is band gap energy (eV) the explored materials. For  $\alpha\text{-Fe}_2\text{O}_3$  ( $E_g = 1.96$  eV),



$\chi$  value is estimated to be 5.88 eV. Table 8 reports  $E_g$ ,  $E_{VB}$  and  $E_{CB}$  values for FMD3 and FMD3X6.

### 3.6. Surface charge

The surface charge of RD, FMD3 and FMD3X6 are estimated by drawing graphs of surface charge vs. pH which is displayed in Fig. 8.  $pH_{PZC}$  values is determined by intersecting three curves with the  $x$ -axis, which was 5.9 for RD, 6 for the both FMD3 and FMD3X6. Thus, the surface charge of diatomite is positive if  $pH < 5.9-6$ , due to the formation of  $SiOH_2^+$ , and negative if  $pH > 5.9-6$ , along with the formation of  $SiO^-$ .

### 3.7. SEM-EDX analysis

In diatoms, there are three types of patterns: centric, pennate, and stereotypes. The SEM micrograph of RD catalyst (Fig. 9a) shows that it was mostly made up of centric type frustules with a honeycomb structure, a diameter of 16.5  $\mu m$ , and a pore diameter of 200–700 nm. The length of the pennate diatom particles ranges from 0.57 to 14.28  $\mu m$ . The length of the stereotypical diatom particles is approximately 1.71–14.28  $\mu m$ . SEM analysis of FMD3 (Fig. 9b)

exhibited the occurrence of ferric oxyhydroxide phases on diatomite frustules [50]. Besides, the SEM micrographs of FMD and FMD3X6 catalyst revealed that raw diatomite frustules are surface modified and the original geometry of the pores is destroyed by the NaOH treatment and

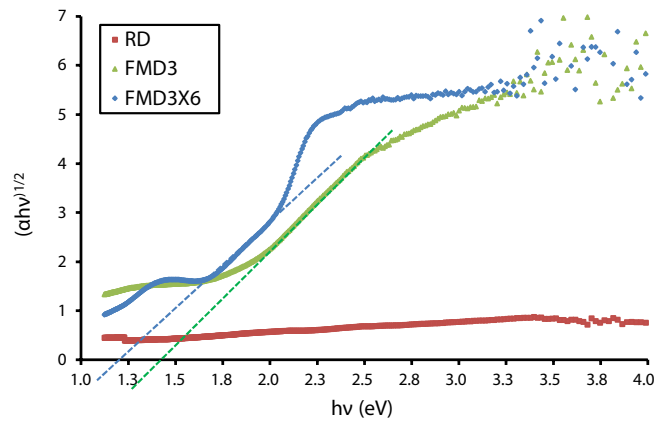


Fig. 7.  $(\alpha h\nu)^{1/2}$  vs.  $(h\nu)$  of RD, FMD3 and FMD3X6.

Table 7  
Optical properties of the VG3, RD, FMD3 and FMD3X6

| Catalyst Abbr. | Absorption onset energy |             | Band gap $E_g$ (eV) |
|----------------|-------------------------|-------------|---------------------|
|                | $\lambda$ (nm)          | $E_g$ (eV)* | Experimental**      |
| VG3            | 310                     | 4           | –                   |
|                | 345                     | 3.59        | –                   |
| RD             | 500–800                 | 2.48–1.55   | –                   |
|                | 500                     | 2.48        | –                   |
| FMD3           | 1,100                   | 1.13        | –                   |
| FMD3           | 875                     | 1.41        | 1.45                |
| FMD3X6         | 975                     | 1.27        | 1.25                |

Abbr.: Abbreviation;

\*:  $E_g$  computed from  $E_g = 1,240/\lambda$ ;

\*\*.:  $E_g$  computed from K.M. method.

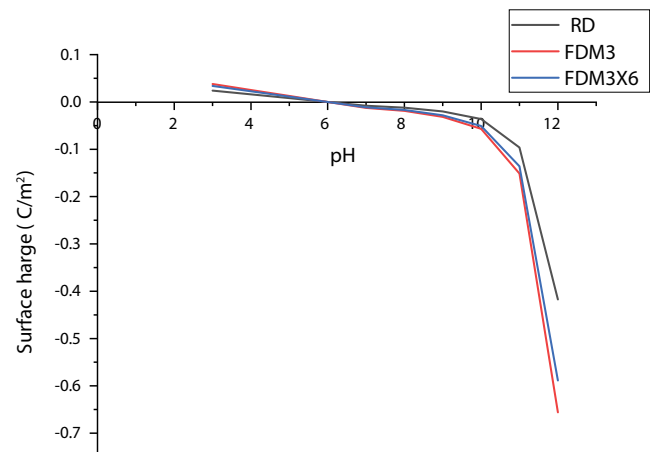


Fig. 8. Surface charge vs pH for RD, FMD3 and FMD3X6.

Table 8  
Optical properties of  $\alpha$ - $Fe_2O_3$ , RD, FMD3 and FMD3X6

| Catalyst Abbr.       | Absorption onset energy |             | Band gap $E_g$ (eV) | $\chi$ (eV) | $E_{VB}$ (eV) | $E_{CB}$ (eV) |
|----------------------|-------------------------|-------------|---------------------|-------------|---------------|---------------|
|                      | $\lambda$ (nm)          | $E_g$ (eV)* | Experimental**      |             |               |               |
| $\alpha$ - $Fe_2O_3$ | –                       | 1.96***     | –                   | 5.88        | –             | –             |
| RD                   | 500                     | 2.48        | –                   | –           | –             | –             |
|                      | 1,000                   | 1.13        | –                   | –           | –             | –             |
| FMD3                 | 875                     | 1.41        | 1.45                | –           | 2.11          | 0.66          |
| FMD3X6               | 975                     | 1.27        | 1.25                | –           | 2.00          | 0.76          |

Abbr.: Abbreviation;

\*:  $E_g$  computed from  $E_g = 1,240/\lambda$ ;

\*\*.:  $E_g$  computed from K.M. method;

\*\*\*.:  $E_g$  computed from literature.



the ferrihydrite deposition (Fig. 9c and d). Colloidal-size ferrihydrite (2–5 nm) is initially deposited in diatomite macropores and/or mesopores.

The elemental analysis of the FMD3 and FMD3X6 are also presented in this study. The EDX plots indicate the composition of element present in the FMD3 (Fig. 9e) and FMD3X6 (Fig. 9f) in term of the percentage weight of elements. FMD3 showed the exact match for standard peak position for Fe (10.20%), O (6.85%), Na (33.98%), Cl (38.77%), C (6.10%), Si (3.53%), Ca (0.53%) and Mg (0.04%) while FMD3X6 exhibited the typical peaks for Fe (50.53%), O (22.41%), Na (19.19%), Cl (18.04%) and Si (8.12%).

### 3.8. XPS analysis

XPS analysis was devoted to describe the chemical composition and electronic states of RD and FMD3X6. As illustrated in Fig. 10, the characteristic survey spectra indicated the occurrence of O, Fe, Si, K and C. In Fig. 10b, Si 2p peak centred at 102.98 eV was attributing to diatomite. In the O1s high-resolution XPS spectrum (Fig. 10c), two peaks centred at 529.5 and 532.22 eV, corresponding to the anionic oxygen from  $^-OH$  group present on the surface FMD3X6 catalyst and the presence of Fe–O–Si or Fe–O–Ti. As shown in Fig. 10d, the binding energy (BE) value peak at 712.4 was ascribed to Fe 2p<sub>1/2</sub> and the peak 724.5 eV related to Fe 2p<sub>3/2</sub>. The energy discrepancy between Fe 2p<sub>1/2</sub> and Fe 2p<sub>3/2</sub> was 12.1 eV, suggesting the presence of Fe<sup>2+</sup> and Fe<sup>3+</sup> states [51]. Furthermore, two small peaks positioned at 718.7 and 733.5 eV corresponded to the Fe shakeup satellite peaks, revealing the presence of a very small amount of  $\gamma$ -Fe<sub>2</sub>O<sub>3</sub> or FeO in the nanocomposites. In Fig. 10e, the high-resolution spectrum of C 1s was presented by two peaks situated at 284.5 eV (C–C) and 288.29 eV (C–O). The high-resolution spectrum of K2p (Fig. 10f) was splitted into positioned at 288.22 eV was assigned to 2p<sub>3/2</sub>, while the peak at 293.92 eV was ascribed to 2p<sub>1/2</sub>. Additionally, for FMD3X6, an extra peak was observed in Fig. 10g corresponding to Cl 2p, and its binding energy at 199 eV correlated to Cl 2p<sub>1/2</sub>. However, further additional peaks were observed in the bare RD. As depicted in Fig. 10h, two representative peaks of Ca ion located at 347.25 and 350.6 eV were accredited to Ca 2p<sub>3/2</sub> and Ca 2p<sub>1/2</sub>, respectively. Moreover, the peak intensity of Na located at 1,071.6 eV was fitted to Na 1s (Fig. 10i). In addition, Al<sub>2</sub>O<sub>3</sub> peak centered at 74.72.6 eV was found in the high resolution Al (2p) spectrum of an aluminium surface (Fig. 10j).

#### 3.8.1. N<sub>2</sub> adsorption–desorption experiments

N<sub>2</sub> adsorption–desorption experiments were conducted to investigate the specific surface area and pore structure of the FMD3X6 catalyst. N<sub>2</sub> adsorption–desorption isotherms and pore-size distribution curves that are illustrated in Figs. 11 and 12, respectively and the detailed results are presented in Table 9. According to the experimental data, as shown in Fig. 11, the isotherms of the as-elaborated catalyst is supposed to be of Type IIa, which indicates that FMD3X6 catalyst is not microporous structures, as evidenced by SEM observation. This observation is consistent with the tendency for hematite to aggregate into platelets [52], and

Table 9  
Summary of BET data for FMD3X6

| Material  | FMD3X6   |
|---|----------|
| BET surface area (m <sup>2</sup> g <sup>-1</sup> )  | 2.1039   |
| Macropore area (m <sup>2</sup> g <sup>-1</sup> )    | –        |
| Mesopore area (m <sup>2</sup> g <sup>-1</sup> )     | –        |
| Micropore area (m <sup>2</sup> g <sup>-1</sup> )    | –1.1344  |
| Total volume (cm <sup>3</sup> g <sup>-1</sup> )     | 0.001    |
| Macropore volume (cm <sup>3</sup> g <sup>-1</sup> ) | –        |
| Mesopore volume (cm <sup>3</sup> g <sup>-1</sup> )  | –        |
| Micropore volume (cm <sup>3</sup> g <sup>-1</sup> ) | 0.000339 |
| Average diameter (nm)                               | 1.90959  |

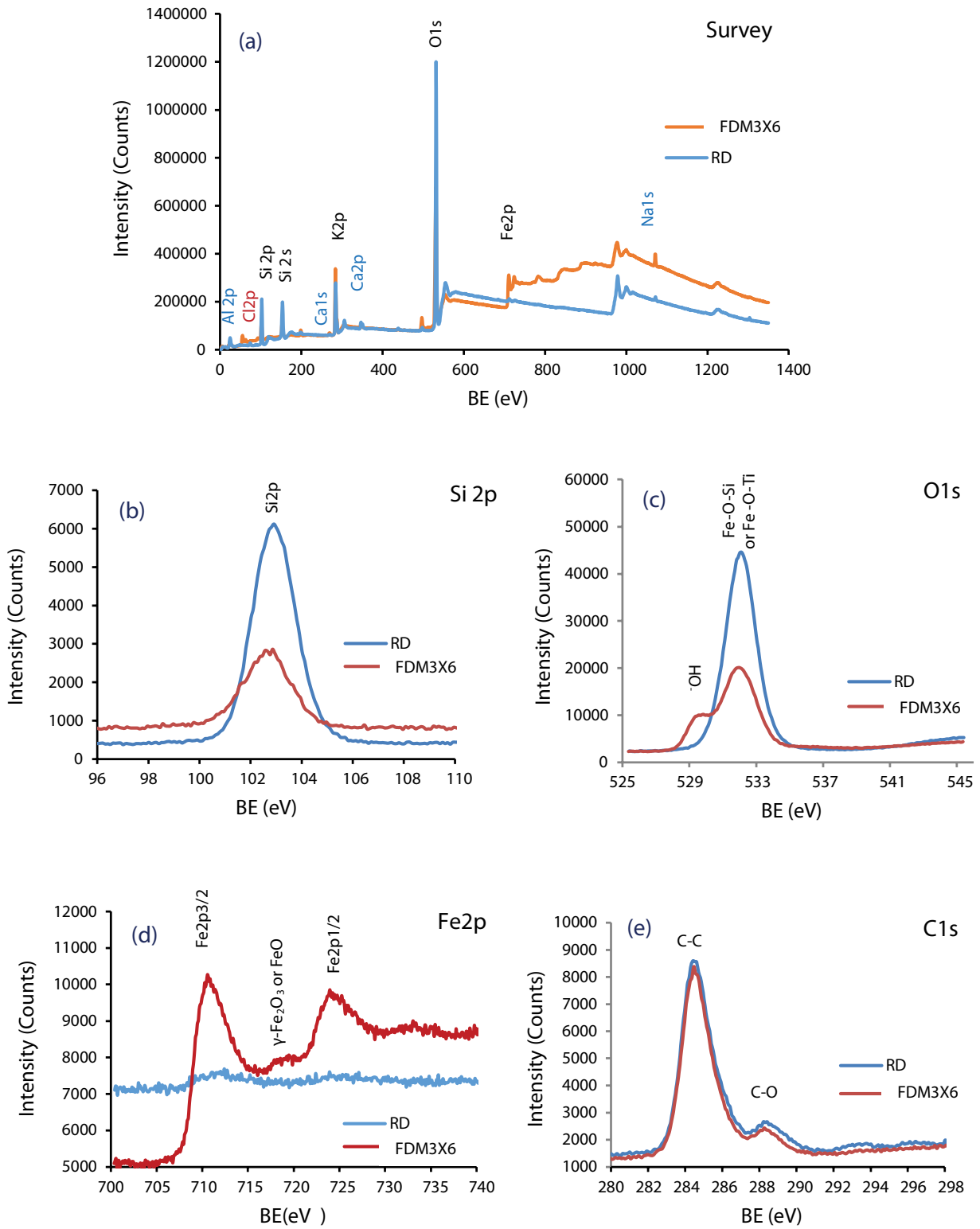
provides further evidence of the presence of hematite ( $\alpha$ -Fe<sub>2</sub>O<sub>3</sub>) platelets on the surface of FMD3X6.

BET specific surface area of the FMD3X6 was assessed to be 2.1 m<sup>2</sup> g<sup>-1</sup>. As depicted in Fig. 6, the pore size shows a sharp shift indicating the predominance of smaller pores. However, the volume of these small pores is less than 10 nm which is attributed to the occurrence presence of  $\alpha$ -Fe<sub>2</sub>O<sub>3</sub>. Moreover, the increase of the micropore region is also illustrated by differential pore-size distributions of FMD3X6 which is defined as  $dV/d(\log D)$ . The term  $V$  represents a cumulative pore volume at a specific average pore diameter. Calculated from the pore-size distribution, the average pore diameter of FMD3X6 is estimated to be 1.9 nm as shown in Table 9.

### 3.9. Photocatalytic activity

#### 3.9.1. Effect of initial pH

The pH of the wastewater is one of the crucial parameters that determine the efficiency of the sorption and the photocatalysis processes under UVA light irradiation. The impact of pH solution on VG3 photodegradation using RD and FMD3X6 as photocatalysts was examined. Thus, the assays were carried out over a range of pH values from 4 to 10 at a fixed VG3 dye concentration (10 mg L<sup>-1</sup>), catalyst dosage (0.5 g L<sup>-1</sup>), at room temperature and at an exposure time of 60 min under UVA (365 nm) light irradiation. The time-dependent pH on the photocatalytic process profiles of RD (Fig. 13a) and FMD3X6 (Fig. 13b) reveal that VG3 was insensitive to the exposure time of 60 min at pH 7 due to the presence of the inactively charged diatomite surface. At this pH = 7, much closer to the diatomite p*H*<sub>PZC</sub> = 5.6–6, the suspension lost its dispersion stability based on principle of general colloid chemistry [53]. As the pH become higher than p*H*<sub>PZC</sub> of diatomite (ca. pH = 10), the negatively charged site on the surface photocatalyst decreased after 60 min, almost reaching pH 8. It was noted that the continuous decrease in pH values leads to the significant increase in the photoactive species via oxidation reaction of H<sub>2</sub>O molecules to  $\cdot OH$  radicals. As the pH becomes lower than p*H*<sub>PZC</sub> (ca. pH = 4), the positively charged site on the surface photocatalyst decreased to pH 6, leading to the increase in the negatively charged site and the photoactive species. Hence, the VG3 degradation is probably enhanced owing to the



(Continued)

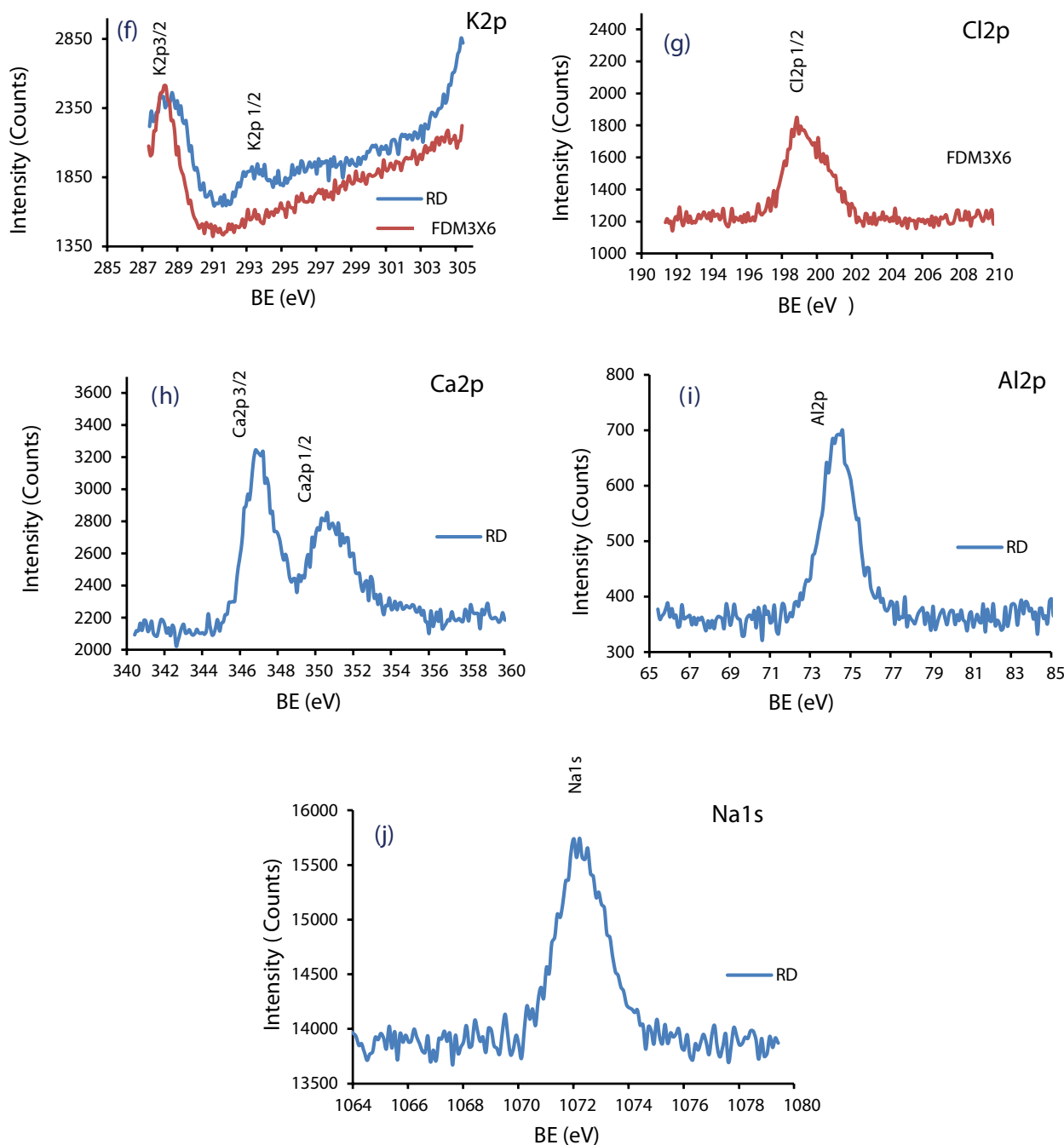


Fig. 10. XPS spectra of RD and FMD3X6. Survey spectra of RD and FMD3X6 (a), high-resolution spectra of (b) Si2p, (c) O 1s, (d) Fe2p, (e) C1s, (f) Cl1s, (g) K2p, (h) Cl2p, (i) Ca2p and (j) Na1s.

presences photoinduced active species via reduction reaction of  $O_2$  to superoxides radicals ( $\cdot O_2^-$ ) [54].

Fig. 14a and b depict plots of  $C/C_0$  vs.  $t$  at various initial pH for RD and FMD3X6, respectively. The photocatalysis equilibrium was reached after 60 min for both photocatalysts. Indeed, FMD3X6 exhibited high photodegradation efficiency, with 79%, 85% and 92% VG3 elimination for pH 4, 7 and 10, respectively, whereas only 74%, 76% and 88% VG3 abatement were achieved for the RD system, at pH 4, 7 and 10, correspondingly.

VG3 molecule is composed of anthraquinonoid, ketonic and amino groups with pKa value of 7.7. So, VG3 presented as cationic form  $H_3OVG3^+$  at pH < 7 and zwitterions ( $H_2OVG3^-$ ) at pH beyond 7.7, due to the loss of hydrogen. Whatever the pH of the solution, electrostatic-repulsion can take place either between  $(Si-O-Fe)OH_3^+$  and  $H_3OVG3^+$  at pH < 7.7 or between  $(Si-O-Fe)O^-$  and  $HOVG3^-$  as pH > 7.7, which reduced the removal capability of RD and FMD3X6. Moreover, as the outermost layer of FMD3X6 consists of  $\alpha-Fe_2O_3$  (and/or  $\gamma-FeOOH$  and  $\gamma-Fe_2O_3$ ) and  $pH_{pzc}$  is



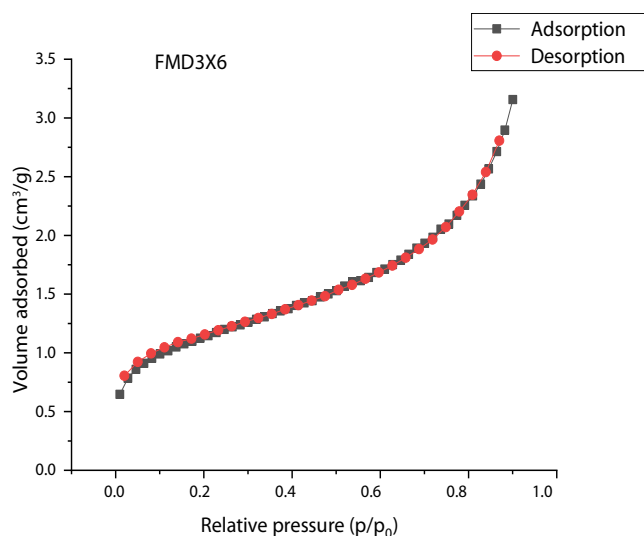


Fig. 11. BET isotherm plots of FMD3X6.

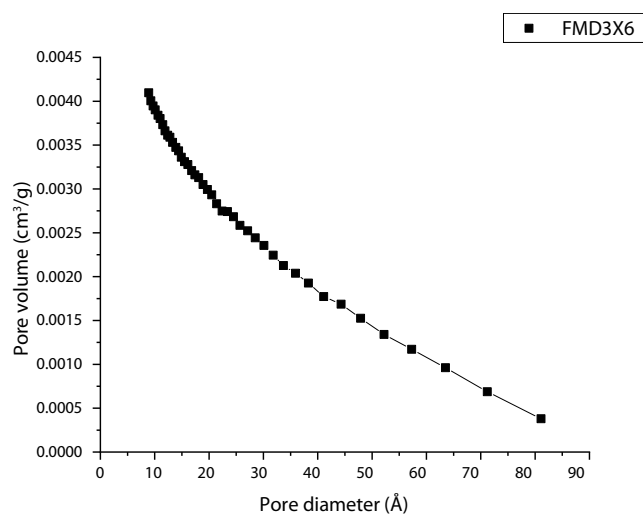


Fig. 12. Differential pore-size distribution and nitrogen adsorption isotherm plot of FMD3X6.

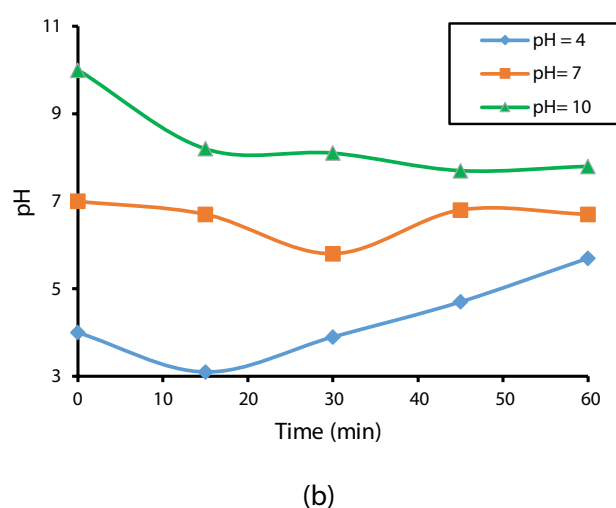
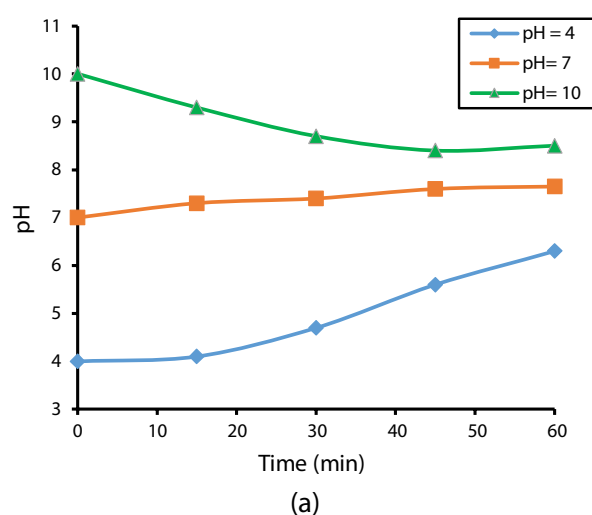


Fig. 13. Time-dependent pH on the photocatalytic process profile of RD (a) and FMD3X6 (b).

7.5 [55], the surface of  $\alpha\text{-Fe}_2\text{O}_3$  is positive ( $\equiv\text{Fe}^{\text{III}}\text{-H}_3\text{O}^+$ ) ( $\text{pH} < 7.5 = \text{pH}_{\text{PZC}}$ ) and negative ( $\equiv\text{Fe}^{\text{III}}\text{-O}^-$ ) ( $\text{pH} > \text{pH}_{\text{PZC}} = 7.5$ ). Such emphasis, leads to the massive transfer of photo-generated electron and holes to the diatomite surfaces, respectively. Thus, oxidizing species  $\cdot\text{O}_2$  (probably) and  $\cdot\text{OH}$  are generated from dissolved  $\text{O}_2$  and  $\text{H}_2\text{O}$ , respectively, through redox reactions mechanism, which enhance the photodecomposition process.

However, at  $\text{pH} = 10$  ( $\text{pH} > \text{pH}_{\text{PZC}} = 7.5$ ), the contribution of  $\text{Na}^+$  ions in the adsorption process could be considered. Indeed,  $\text{Na}^+$  can act as a cation bridge between the negatively charged  $\text{VG}3^-$  and  $\text{SiO}^-$ , possibly forming a complex  $[(\text{Si}-\text{O}-\text{Fe})\text{O}^- \cdots \text{Na}^+ \cdots \text{VG}3^-]$  or  $[(\equiv\text{Fe}^{\text{III}}\text{-O}^- \cdots \text{Na}^+ \cdots \text{VG}3^-)]$ , facilitating greater dye adsorption. Thus, the degradation efficiency of FMD3X6 towards the VG3 species enhanced greatly at  $\text{pH} = 10$  [56].

However, at  $6 \leq \text{pH} \leq 7.7$ , most of the VG3 was protonated and the both photocatalysts (RD and FMD3X6)

diatomite surfaces were similarly deprotonated, resulting in higher electrostatic attraction between  $\text{H}_3\text{OVG}3^+$  and  $\text{SiO}^-$ , which is the main reason for the visible difference in the degradation efficiencies between RD and FMD3X6. This highlight is in dissimilar tendency to the principle of general colloid chemistry. Indeed, at  $\text{pH}$  close to  $\text{pH}_{\text{PZC}}$  of diatomites (5.6–6), a loss of stability dispersion of the particle was occurred. Thus, the particles may agglomerate rapidly by increasing the particle size and reducing positive site of surface catalyst.

As the  $\text{pH}$  becomes lower than  $\text{pH}_{\text{PZC}}$  values of FMD3X6 and  $\alpha\text{-Fe}_2\text{O}_3$  (ca.  $\text{pH} = 4$ ), the  $\alpha\text{-Fe}_2\text{O}_3$  ( $\equiv\text{Fe}^{\text{III}}\text{-H}_3\text{O}^+$ ), FMD3X6 ( $(\text{Si}-\text{O}-\text{Fe})\text{OH}_3^+$ ) and  $\text{H}_3\text{OVG}3^+$  surface are all positively charged. The electrostatic-repulsion interactions may take place either between  $\equiv\text{Fe}^{\text{III}}\text{-H}_3\text{O}^+$  and  $\text{H}_3\text{OVG}3^+$  or between the positively charged  $(\text{Si}-\text{O}-\text{Fe})\text{OH}_3^+$  and  $\text{H}_3\text{OVG}3^+$ , which may harmfully affect the adsorption extent as well the photodegradation process. Moreover,  $\alpha\text{-Fe}_2\text{O}_3$  particles are



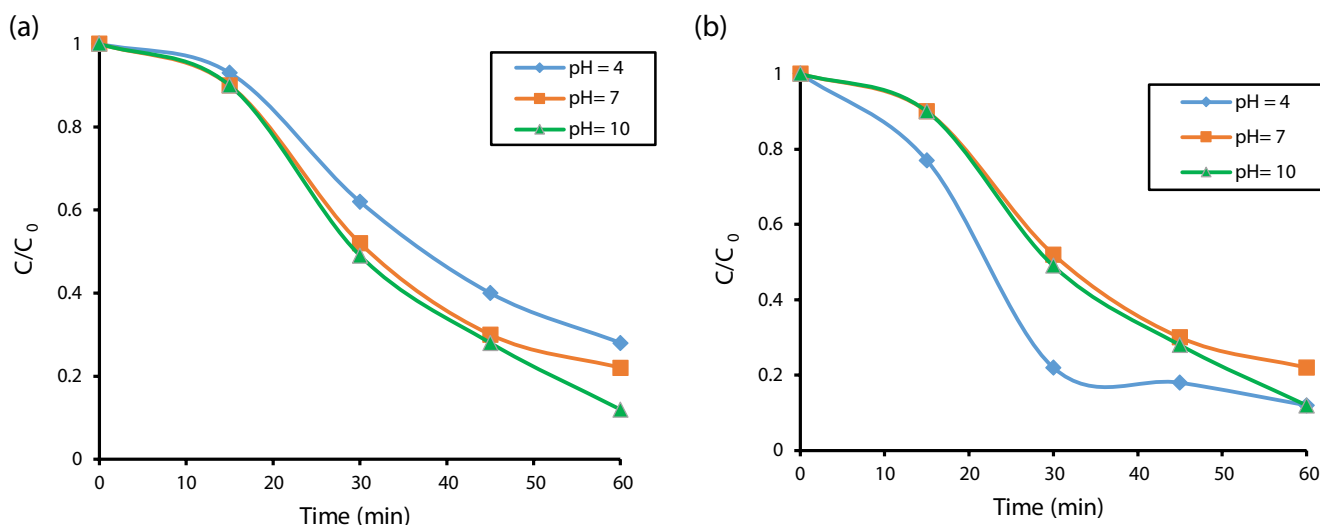


Fig. 14. Kinetics of VG3 photodegradation at various pH using (a) RD and (b) FMD3X6.

more sensitive to the pH medium. As we know that  $pH_{PZC}$  of  $\alpha\text{-Fe}_2\text{O}_3$  is 7.5, suggesting the particle sizes of  $\alpha\text{-Fe}_2\text{O}_3$  are smaller at lower pH than at neutral pH and the agglomeration of the  $\alpha\text{-Fe}_2\text{O}_3$  particles increased as the pH increased from 4 to 7.  $\alpha\text{-Fe}_2\text{O}_3$  particles in the acidic medium solution (ca. pH = 4) are dispersing, but are getting agglomerating as the pH is increasing up to 7 and above (ca. pH = 10). At pH 4.0, the suspension is intrinsically stable and more dispersible, while precipitation then agglomeration may gradually occurred at pH values close to 7. These highlights prove that the size of the NPs depends on the pH. Thus, lower pH values result in a smaller particle size of  $\alpha\text{-Fe}_2\text{O}_3$  which can be an important factor for enhancing transfer and mobility of the photoinduced electrons to the surface of the diatomites materials, thus, to the transfer of photo-generated electron to the diatomite surfaces. Thus, improving oxidizing species such as  $\cdot\text{OH}$  radicals are generated from dissolved  $\text{O}_2$  through reduction reaction mechanism, which enhance the photodecomposition process of VG3 over FMD3X6 [57].

The slight discrepancy in the degradation efficiencies for RD and FMD3X6 especially at pH = 10 can be explained to the intrinsic and unique features of FMD3X6 material. Although its low surface area ( $218.2$  vs  $307.8$   $\text{m}^2$   $\text{g}^{-1}$ ) compared to the RD and decreased CaO, MgO,  $\text{K}_2\text{O}$ ,  $\text{SO}_3$  and  $\text{P}_2\text{O}_5$  impurities ratios, possibly acting as recombination center, the reduced band gap value from  $1.25$  eV (FMD3X6) to  $2.48$  eV (RD), plays a positive impact towards stimulating of the FMD3X6 in visible light region. Moreover, the  $\text{Fe}^{2+}/\text{Fe}^{3+}$  ratio and  $\cdot\text{OH}$  group on the surface FMD3X6, as evidenced by XPS analysis, were greatly boosted and more reactive oxygen species (ROS) such as  $\cdot\text{OH}$  were then produced via radical oxidation mechanism, which is primary responsible for the cleavage and oxidation of dye molecules as well the efficient degradation. However, the depleted  $\text{SiO}_2$  ratio from  $68.02\%$  (FMD3X6) to  $37.27\%$  (RD) results in a relative solubility in the alkali medium and loss of the dispersion stability of particles FMD3X6.

### 3.9.2. Kinetics modeling

Fig. 15 depicts the linear fitting of  $\ln C/C_0$  vs.  $t$  of VG3 degradation of using RD (Fig. 15a) and FMD3X6 (Fig. 15b) at various pH. The apparent reactions rate constant ( $K_1$ ) and regression coefficient ( $R^2$ ) of each pH were calculated and summarized in Table 10. The photodegradation kinetic obeys the pseudo-first-order reaction. All experiments demonstrated that RD ( $\eta = 88\%$ ) and FMD3X6 ( $\eta = 92\%$ ) exhibit a substantial photocatalytic efficiency at pH = 10. For the RD, with increasing pH from 4 to 10,  $K_1$  increases from  $1.97 \times 10^{-2}$  to  $3.07 \times 10^{-2}$   $\text{min}^{-1}$ , respectively. Meanwhile, FMD3X6 showed  $K_1$  similar to that of RD at pH = 7 ( $K_1 = 2.46 \times 10^{-2}$   $\text{min}^{-1}$ ) and pH = 10 ( $K_1 = 3.07 \times 10^{-2}$   $\text{min}^{-1}$ ). However, at pH = 4,  $K_1$  of FMD3X6 ( $K_1 = 3.76 \times 10^{-2}$   $\text{min}^{-1}$ ) was almost 2 times higher than that of RD support ( $K_1 = 1.97 \times 10^{-2}$   $\text{min}^{-1}$ ), demonstrating the best photocatalytic response. The regression coefficient ( $R^2$ ) values are  $>0.92$  for all experiments.

### 3.9.3. Effect of different surface areas catalytic performances of RD, FMD3 and and FMD3X6?

The average crystallite size of RD, FMD3 and FMD3X6 are  $106.105$ ,  $90.890$  and  $116.448$  nm, respectively. Meanwhile, according to the Sears process, the surface area value of RD ( $307.8$   $\text{m}^2$   $\text{g}^{-1}$ ) was higher than these of FMD3 ( $195.8$   $\text{m}^2$   $\text{g}^{-1}$ ) and FMD3X6 ( $218.2$   $\text{m}^2$   $\text{g}^{-1}$ ). Although to the dissimilarity in the surface area values of diatomites, FMD3X6 annealed up to  $600^\circ\text{C}$  for 24 h, exhibited a slight superiority in the photodegradation efficiency at various pH. From the above results, it is clear that two requirements, namely, a good crystallinity and large surface area, are wholly satisfied by heat treatment at  $600^\circ\text{C}/24$  h, as well as the presence of the  $\text{Fe}^{2+}/\text{Fe}^{3+}$  fraction on the surface FMD3X6, as evidenced by XPS analysis. Annealing process, often give rise to particle agglomeration with severe loss of effective surface area. Thus, FMD3X6 particles tend to agglomerate during the heat treatment process due to the

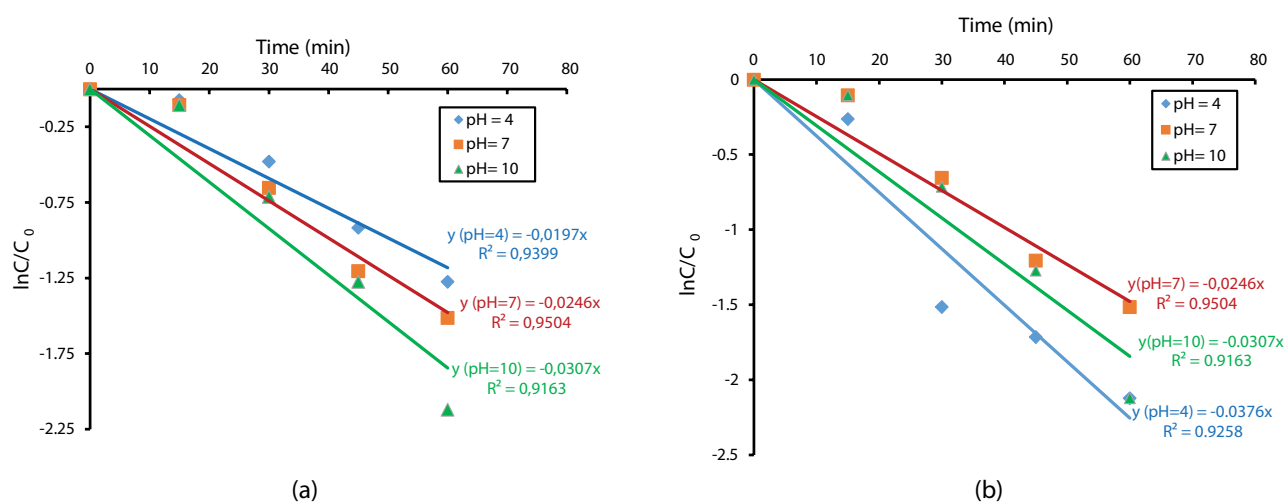


Fig. 15. Linear plot of  $\ln(C/C_0)$  vs.  $t$  of photocatalytic degradation at various pH (a) RD and (b) FMD3X6.

Table 10

Pseudo-first-order kinetic parameters of photocatalytic degradation at various pH using RD and FMD3X6

| pH | Catalyst Abbr. | $\eta$ (%) | $K$ ( $\text{min}^{-1}$ ) $\times 10^2$ | $t^{1/2}$ (min) | $R^2$ |
|----|----------------|------------|---|-----------------|-------|
| 4  | RD             | 74         | 1.97                                    | 35.18           | 0.94  |
| 7  | RD             | 76         | 2.46                                    | 28.17           | 0.95  |
| 10 | RD             | 88         | 3.07                                    | 22.57           | 0.92  |
| 4  | FMD3X6         | 79         | 3.76                                    | 18.43           | 0.93  |
| 7  | FMD3X6         | 85         | 2.46                                    | 28.17           | 0.95  |
| 10 | FMD3X6         | 92         | 3.07                                    | 22.57           | 0.92  |

Abbr.: Abbreviation;

$\eta$ : Photocatalytic efficiency.

van der Waals attraction forces. However, its crystallinity is enhanced by the presence of iron species and the decrease in CaO, MgO, K<sub>2</sub>O, SO<sub>3</sub> and P<sub>2</sub>O<sub>5</sub> impurities ratios which act as recombination sites of photo-excited electron-hole.

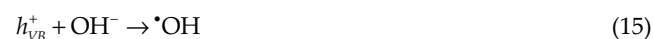
As a result, the crystallinity of the FMD3X6 catalyst is improved by annealing at 600°C/24 h. It can reduce the diffusion path length for the charge carriers, which results in a reduced recombination rate of photogenerated carriers and enhances the probability of light-generated carriers transfer via interfaces spatially available, and therefore can improve the photocatalytic activity of a FMD3X6.

### 3.9.4. Photocatalytic mechanism

The probable mechanism scheme of photocatalytic activity of FMD3X6 on the degradation of VG3 is shown in Fig. 16. UVA light energy is sufficient to stimulate FMD3X6 ( $E_g = 1.25$  eV). Under UVA light ( $E_{hv} = 3.39$  eV) illumination, photo-induced charge pairs (electron ( $e^-$ ) in CB and holes ( $h^+$ ) in the VB) were produced over the surface of FMD3X6 [Eq. (13)]:

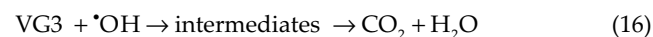


Because of the redox potentials of  $\text{O}_2/\text{O}_2^{\cdot-}$  ( $-0.33$  V/NHE) and  $\text{O}_2/\cdot\text{OH}$  ( $+0.7$  V vs. NHE) are respectively much more negative and slightly positive than the CB edge potential of FMD3X6 ( $+0.76$  eV/NHE), the photo-induced  $e_{\text{CB}}^-$  cannot reduce  $\text{O}_2$  to  $\text{O}_2^{\cdot-}$ , but can directly reduce dissolved  $\text{O}_2$  to  $\cdot\text{OH}$  radicals [Eq. (11)]. Meanwhile, the photo-generated  $h_{\text{VB}}^+$  react with  $\text{OH}^-$  groups which act as donor species to yield  $\cdot\text{OH}$  [Eq. (14)] due to the VB edge energies of FMD3X6 ( $+2.00$  eV/NHE) is slightly more positive than the standard potential of  $\text{OH}^-/\cdot\text{OH}$  ( $+1.99$  eV/NHE).



In the contrast, these photo-excited holes cannot subsequently oxidise the  $\text{H}_2\text{O}$  to  $\cdot\text{OH}$  radicals, as the VB of the FMD3X6 is more negative than the oxidation potential of  $\text{H}_2\text{O}/\cdot\text{OH}$  ( $+2.8$  V/NHE).

Thus, the generated radicals,  $h^+$  and  $\cdot\text{OH}$ , as powerful oxidizing agents, attack organic molecules causing the chain cleavage and oxidation reactions of dye molecules [58] [Eq. (15)].



## 4. Conclusion

Ferrihydrite immobilized on diatomite was developed in the present study. Results revealed that FMD3X6 possessed multi crystalline phases:  $\text{SiO}_2$ ,  $\gamma\text{-FeOOH}$ ,  $\alpha\text{-Fe}_2\text{O}_3$ ,  $\gamma\text{-Fe}_2\text{O}_3$  and  $\text{CaCO}_3$ . The average crystallite size of RD, FMD3 and FMD3X6 were 106.105, 90.890 and 116.448 nm, respectively. On the base of the Sears process, the surface area of RD ( $307.8$   $\text{m}^2$   $\text{g}^{-1}$ ) was higher compared to the than of FMD3 ( $195.8$   $\text{m}^2$   $\text{g}^{-1}$ ) and FMD3X6 ( $218.2$   $\text{m}^2$   $\text{g}^{-1}$ ). The band gap values were 2.48, 1.45 and 1.25 eV for RD, FMD3 and FMD3X6, respectively, while the  $\text{pH}_{\text{PZC}}$  were found

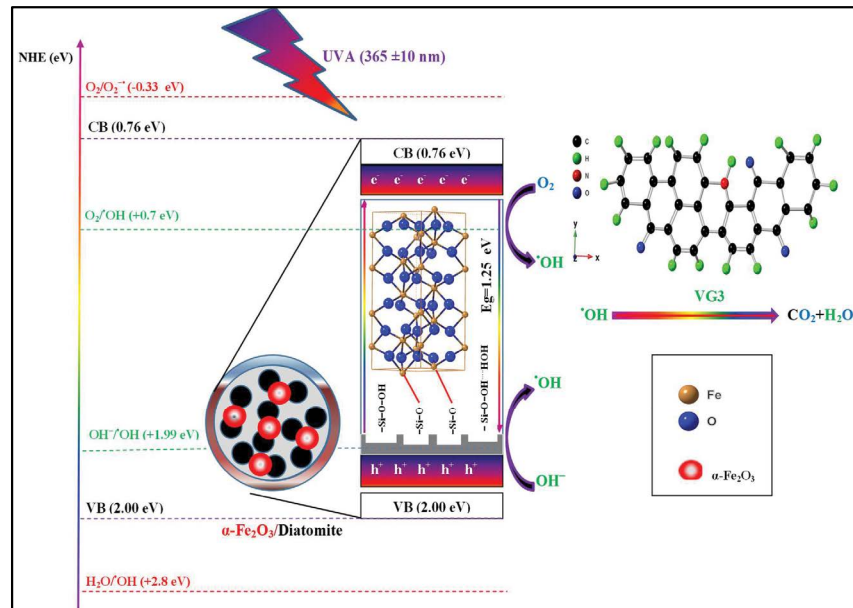


Fig. 16. Proposed mechanism of photocatalytic degradation of VG3 over FMD3X6 catalyst under the UVA light irradiation.

to be 5 for RD and 6 for the both FMD3 and FMD3X6. SEM-EDS study indicated a good distribution of ferrihydrite on surface of diatomite frustules. Moreover, comparing the binding energies of Fe  $2p_{1/2}$ , Fe  $2p_{3/2}$  and O 1s of FMD3X6 with RD, it is implied that  $\alpha\text{-Fe}_2\text{O}_3$  is combined as Fe–O–Si bond. BET specific surface area of the FMD3X6 was assessed to be  $2.1 \text{ m}^2 \text{ g}^{-1}$ . The predicted average pore diameter of FMD3X6 is estimated to be 1.9 nm. Up to 92% degradation of VG3 was achieved within 1h at pH = 10 at 25°C using FMD3X6, which was a slightly better efficiency than pristine diatomite; RD (88% degradation of VG3). The photodegradation process well described by the pseudo-first-order kinetic model ( $R^2 > 0.9$ ). The enhanced photocatalytic performance of the FMD3X6 system is attributed to the generated powerful oxidizing agents ( $\text{h}^+$  and  $\cdot\text{OH}$ ), which attack organic molecules causing the chain cleavage and oxidation reactions of dye molecules.

### Acknowledgements

The authors are thankful to the General Direction of Scientific Research (DGRSDT-Algeria).

### References

- [1] J. Clarke, The occurrence and significance of biogenic opal in the regolith, *Earth Sci. Rev.*, 60 (2003) 175–194.
- [2] L.A. Benzelmatt, R. Cherraka, M. Hadjel, A. Ketteb, N. Goual, Characterization between crude diatomite and diatomite treated chemically, *Algerian J. Environ. Sci. Technol.*, 5 (2019) 1107–1112.
- [3] H. Meradi, L. Atoui, W. Ghabeche, L. Bahloul, Contribution to characterization of natural diatomite, *Int. J. Sci. Res. Eng. Technol. (IJSET)*, 9 (2019) 6–11.
- [4] M.P. Cabrera, C.R.D. Assis, D.F.M. Neri, C.F. Pereira, F. Soria, B.L. Carvalho Jr., High sucrolytic activity by invertase immobilized onto magnetic diatomaceous earth nanoparticles, *Biotechnol. Rep.*, 14 (2017) 38–46.
- [5] B. Wang, F.C. de Godoi, Z. Sun, Q. Zeng, S. Zheng, R.L. Frost, Synthesis, characterization and activity of an immobilized photocatalyst: natural porous diatomite supported titania nanoparticles, *J. Colloid Interface Sci.*, 438 (2015) 204–211.
- [6] T. Benkacem, B. Hamdi, A. Chamayou, H. Balard, R. Calvet, Physicochemical characterization of a diatomaceous upon an acid treatment: a focus on surface properties by inverse gas chromatography, *Powder Technol.*, 294 (2016) 498–507.
- [7] H. Hadjar, B. Hamdi, M. Jaber, J. Brendlé, Z. Kessaïssia, H. Balard, J.B. Donnet, Elaboration and characterisation of new mesoporous materials from diatomite and charcoal, *Microporous Mesoporous Mater.*, 107 (2008) 219–226.
- [8] M. Sprynskyy, I. Kovalchuk, B. Buszewski, The separation of uranium ions by natural and modified diatomite from aqueous solution, *J. Hazard. Mater.*, 181 (2010) 700–707.
- [9] M. Šljivić, I. Smičiklas, S. Pejanović, I. Plečaš, Comparative study of  $\text{Cu}^{2+}$  adsorption on a zeolite, a clay and a diatomite from Serbia, *Appl. Clay Sci.*, 43 (2009) 33–40.
- [10] P. Yuan, D. Liu, D.-Y. Tan, K.-K. Liu, H.-G. Yu, Y.-H. Zhong, A.-H. Yuan, W.-B. Yu, H.-P. He, Surface silylation of mesoporous/macroporous diatomite (diatomaceous earth) and its function in Cu(II) adsorption: the effects of heating pretreatment, *Microporous Mesoporous Mater.*, 170 (2013) 9–19.
- [11] L. Sun, J. Wang, J. Wu, T. Wang, Y. Du, Y. Li, H. Li, Constructing nanostructured silicates on diatomite for Pb(II) and Cd(II) removal, *J. Mater. Sci.*, 54 (2019) 6882–6894.
- [12] Y. Du, X. Wang, J. Wu, J. Wang, Y. Li, H. Dai,  $\text{Mg}_3\text{Si}_4\text{O}_{10}(\text{OH})_2$  and  $\text{MgFe}_2\text{O}_4$  in situ grown on diatomite: highly efficient adsorbents for the removal of Cr(VI), *Microporous Mesoporous Mater.*, 271 (2018) 83–91.
- [13] N. Liu, Y. Wu, H. Sha, Magnesium oxide modified diatomite waste as an efficient adsorbent for organic dye removal: adsorption performance and mechanism studies, *Sep. Sci. Technol.*, 55 (2020) 234–246.
- [14] M.B. Nguyen, T.V. Nguyen, G.H. Le, T.T.T. Pham, K.L. Van, G.T.T. Pham, T.N. Nguyen, Q.V. Tran, T.A. Vu, High CO adsorption performance of CuCl-modified diatomites by using the novel method “Atomic Implantation”, *J. Chem.*, 2021 (2021) 9762578, doi: 10.1155/2021/9762578.
- [15] S. Chentouf, Modification des Diatomites et Bentonites Algériennes par des Espèces Chimiques Minérales et Organiques. Synthèses, Caractérisation et Applications, Thesis 2020.

- [16] T. Wang, Y. Yang, J. Wang, J. Wu, L. Sun, Y. Du, Y. Li, H. Li. A general route to modify diatomite with niobates for versatile applications of heavy metal removal, *RSC Adv.*, 9 (2019) 3816–3827.
- [17] Y. Fu, Y. Huang, J. Hu, Z. Zhang, Preparation of chitosan/amine modified diatomite composites and adsorption properties of Hg(II) ions, *Water Sci. Technol.*, 77 (2018) 1363–1371.
- [18] K.-J. Hsien, W.-T. Tsai, T.-Y. Su, Preparation of diatomite–TiO<sub>2</sub> composite for photodegradation of bisphenol-A in water, *J. Sol-Gel Sci. Technol.*, 51 (2009) 63–69.
- [19] Z. Sun, C. Bai, S. Zheng, X. Yang, R.L. Frost, A comparative study of different porous amorphous silica minerals supported TiO<sub>2</sub> catalysts, *Appl. Catal.*, A, 458 (2013) 103–110.
- [20] S.K. Padmanabhan, S. Pal, E. UIHaq, A. Licciulli, Nanocrystalline TiO<sub>2</sub>-diatomite composite catalysts: effect of crystallization on the photocatalytic degradation of rhodamine B, *Appl. Catal.*, A, 485 (2014) 157–162.
- [21] S.K. Padmanabhan, S. Pal, A. Licciulli, Diatomite/silver phosphate composite for efficient degradation of organic dyes under solar radiation, *Bull. Mater. Sci.*, 43 (2020) 295, doi: 10.1007/s12034-020-02269-2.
- [22] H.-T. Zhu, Q.-F. Ren, Z. Jin, Y. Ding, X.-Y. Liu, X.-H. Ni, M.-L. Han, S.-Y. Ma, Q. Ye, W.-C. Oh, Preparation of AgCl/Ag<sub>3</sub>PO<sub>4</sub>/diatomite composite by microemulsion method for rapid photo-degradation of rhodamine B with stability under visible light, *Korean J. Mater. Res.*, 30 (2020) 383–392.
- [23] W. Rezig, M. Hadjel, Visible light assisted heterogeneous photocatalysis of vat orange 02 textile dye in aqueous solution using calcined ferrihydrite-modified diatomite, *Int. J. ChemTech. Res.*, 8 (2015) 111–115.
- [24] U. Nahr, W. von Bistram, Foundations for the computer-aided calculation of chemicals for dyeing with indanthrene dyes in partly or fully-flooded closed pressure dyeing machines, *Text. Praxis Int.*, 46 (1991) 978–983.
- [25] F. Govaert, E. Temmerman, P. Westbroek, Determination of anthraquinone in alkaline sodium dithionite solution by electrochemical analysis, *Anal. Commun.*, 35 (1998) 153–156.
- [26] M. Anbu Kulandainathan, K. Patil, A. Muthukumar, R.B. Chavan, Review of the process development aspects of electrochemical dyeing: its impact and commercial applications, *Color. Technol.*, 123 (2007) 143–151.
- [27] A. Roessler, D. Crettenand, Direct electrochemical reduction of vat dyes in a fixed bed of graphite granules, *Dyes Pigm.*, 63 (2004) 29–37.
- [28] W. Rezig, M. Hadjel, Photocatalytic degradation of vat green 3 textile dye, using the ferrihydrite-modified diatomite with TiO<sub>2</sub>/UV process, *Orient. J. Chem.*, 30 (2014) 993–1007, doi: 10.13005/ojc/300310.
- [29] R.O.Y. Breese, Diatomite, D.D. Carr, Ed., *Industrial Minerals and Rocks*, SMME, Colorado, USA, 1994, pp. 397–412.
- [30] U. Schwertmann, R.M. Cornell, *Iron Oxides in the Laboratory: Preparation and Characterization*, Wiley-VCH, New York, 2000.
- [31] G.W. Sears, Determination of specific surface area of colloidal silica by titration with sodium hydroxide, *Anal. Chem.*, 28 (1956) 1981–1983.
- [32] Y. Al-Degs, M.A.M. Khraisheh, M.F. Tutunji, Sorption of lead ions on diatomite and manganese oxides modified diatomite, *Water Res.*, 35 (2001) 3724–3728.
- [33] J. Chen, S. Yiacoumi, T.G. Blaydes, Equilibrium and kinetic studies of copper adsorption by activated carbon, *Sep. Technol.*, 6 (1996) 133–146.
- [34] J. Paul Chen, M. Lin, Equilibrium and kinetics of metal ion adsorption onto a commercial H-type granular activated carbon: experimental and modeling studies, *Water Res.*, 35 (2001) 2385–2394.
- [35] P. Yuan, D.Q. Wu, H.P. He, Z.Y. Lin, The hydroxyl species and acid sites on diatomite surface: a combined IR and Raman study, *Appl. Surf. Sci.*, 227 (2004) 30–39.
- [36] B. Xu, Z. Li, Paraffin/diatomite composite phase change material incorporated cement-based composite for thermal energy storage, *Appl. Energy*, 105 (2013) 229–237.
- [37] R. Yezou, Contribution à l'étude des propriétés thermoplastiques des matériaux de construction cohérents et non cohérents, Thèse de Docteur-Ingénieur, INSA de Lyon, France, 1978.
- [38] W. Xu, D.B. Hausner, R. Harrington, P.L. Lee, D.R. Strongin, J.B. Parise, Structural water in ferrihydrite and constraints this provides on possible structure models, *Am. Mineral.*, 96 (2011) 513–520.
- [39] A. Rufus, N. Sreeju, V. Vilas, D. Philip, Biosynthesis of hematite (α-Fe<sub>2</sub>O<sub>3</sub>) nanostructures: size effects on applications in thermal conductivity, catalysis, and antibacterial activity, *J. Mol. Liq.*, 242 (2017) 537–549.
- [40] A. Lassoued, B. Dkhil, A. Gadri, S. Ammar, Control of the shape and size of iron oxide (α-Fe<sub>2</sub>O<sub>3</sub>) nanoparticles synthesized through the chemical precipitation method, *Results Phys.*, 7 (2017) 3007–3015.
- [41] M. Stoia, A. Tamaş, G. Rusu, J. Moroşanu, Synthesis of magnetic iron oxides from ferrous sulfate and substitutes amines, *Stud. Univ. Babeş-Bolyai Chem.*, 61 (2016) 147–162.
- [42] V. Rao, A.L. Shashimohan, A.B. Biswas, Studies on the formation of γ-Fe<sub>2</sub>O<sub>3</sub> (maghemite) by thermal decomposition of ferrous oxalate hydrate, *J. Mater. Sci.*, 9 (1974) 430–433.
- [43] R. Cornell, U. Schwertmann, *Structure, Properties, Reactions, Occurrence and Uses*, VCH, Weinheim, 1996.
- [44] H. Böke, S. Akkurt, S. Özdemir, E.H. Göktürk, E.N.C. Saltik, Quantification of CaCO<sub>3</sub>-CaSO<sub>3</sub>·0.5H<sub>2</sub>O-CaSO<sub>4</sub>·2H<sub>2</sub>O mixtures by FTIR analysis and its ANN model, *Mater. Lett.*, 58 (2004) 723–726.
- [45] B.A. Morrow, I.D. Gay, *Adsorption on Silica Surfaces*, E. Papirer, M. Dekker, Ed., Institut de Chimie des Surfaces et Interfaces, Mulhouse, France, Taylor & Francis Group, CRC Press, Boca Raton, London, New York, ISBN: 0-8247-0003-1, 2000, pp. 9–33.
- [46] W. Xu, D.B. Hausner, R. Harrington, P.L. Lee, D.R. Strongin, J.B. Parise, Structural water in ferrihydrite and constraints this provides on possible structure models, *Am. Mineral.*, 96 (2011) 513–520.
- [47] E. Abdelkader, L. Nadjia, B. Naceur, L. Favier-Teodorescu, Thermal, structural and optical properties of magnetic BiFeO<sub>3</sub> micron-particles synthesized by coprecipitation method: heterogeneous photocatalysis study under white LED irradiation, *Cerâmica*, 68 (2022) 84–96.
- [48] M. Muruganandham, M. Swaminathan, Decolorisation of Reactive Orange 4 by Fenton and photo-Fenton oxidation technology, *Dyes Pigm.*, 63 (2004) 315–321.
- [49] N. Laouedj, A. Elaziouti, N. Benhadria, A. Bekka, CeO<sub>2</sub> nanoscale particles: synthesis, characterization and photocatalytic activity under UVA light irradiation, *J. Rare Earths*, 36 (2018) 575–587.
- [50] X. Yang, X. Zhang, Y. Ma, Y. Huang, Y. Wang, Y. Chen. Superparamagnetic graphene oxide-Fe<sub>3</sub>O<sub>4</sub> nanoparticles hybrid for controlled targeted drug carriers, *J. Mater. Chem.*, 19 (2009) 2710–2714.
- [51] T. Yamashita, P. Hayes, Analysis of XPS spectra of Fe<sup>2+</sup> and Fe<sup>3+</sup> ions in oxide materials, *Appl. Surf. Sci.*, 254 (2008) 2441–2449.
- [52] E. Matijevic, M. Borkovec, *Surface and Colloid Surface*, Springer, Boston, 2004.
- [53] N. Benhadria, A. Elaziouti, N. Laouedj, E. Sari, NZF nanoscale particles: synthesis, characterization and its effective adsorption of bromophenol blue, *Bull. Chem. React. Eng. Catal.*, 15 (2020) 726–742.
- [54] H. Jiang, R. Wang, D. Wang, X. Hong, S. Yang, SnO<sub>2</sub>/diatomite composite prepared by solvothermal reaction for low-cost photocatalysts, *Catalysts*, 9 (2019) 1060, doi: 10.3390/catal9121060.
- [55] H.F. Moafil, R. Ansari, S. Sadeghnia, Preparation of wood sawdust/Fe<sub>3</sub>O<sub>4</sub> nanocomposite and its application for arsenic(III) ion removal from aqueous solutions, *Cellul. Chem. Technol.*, 52 (2018) 271–282.
- [56] A. Elaziouti, N. Laouedj, N. Benhadria, L. Favier-Teodorescu, Thermal, structural and optical properties of magnetic BiFeO<sub>3</sub> micron-particles synthesized by coprecipitation method: heterogeneous photocatalysis study under white LED irradiation, *Cerâmica*, 68 (2022) 84–96.
- [57] X. Meng, J. Ryu, B. Kim, S. Ko, Application of iron oxide as a pH-dependent indicator for improving the nutritional quality, *Clin. Nutr. Res.*, 5 (2016) 172–179.
- [58] L. Favier, A.M. Sescu, A. Elaziouti, L. Oughebbi Berthou, D. Lutic, Urea-assisted synthesis of mesoporous TiO<sub>2</sub> photocatalysts for the efficient removal of clofibric acid from water, *Materials*, 14 (2021) 6035, doi: 10.3390/ma14206035.